Glaciers and Ice Sheets Interferometric Radar

A NASA Instrument Incubator Project

NNG05GL47G

Year-1 Summary and Year-2 Budget Request

Prepared by:

Kenneth C. Jezek, Principal Investigator
C. Allen, J. Curlander, P. Gogineni, P. Kanagaratnam, E Rodriguez and J. Sonntag, Co-Investigators

Submitted to:

Dr. Eduardo Torres-Martinez
Earth Science Technology Office
Goddard Space Flight Center
The National Aeronautics and Space Administration

May 25, 2006

Requested Amount for Year 2:

The Ohio State University:	$622,117
JPL:	$295,100
Wallops Flight Facility:	$150,000

Period: July 1, 2006 – June 30, 2007

Table of Contents

1.0 Introduction

The Global Ice Sheet Interferometric Radar (GISIR) project is tasked with developing and demonstrating a novel concept for measuring the surface and basal topography of terrestrial ice sheets and determining the physical properties of the glacier bed. The primary technical goal of the project is to develop and demonstrate methods for isolating VHF and UHF radar returns from the ice-bed interface from those from the ice surface. The primary science objective is to develop this new technology for obtaining spaceborne estimates of the thickness of the polar ice sheets with an ultimate goal of providing essential information to modelers estimating the mass balance of the polar ice sheets and estimating the response of ice sheets to changing climate.

Our approach is designed to reduce signal contamination from surface clutter, measure the topography of the glacier bed at better than 1 km intervals with an accuracy of 20 m, and paint a picture of variations in bed characteristics. The technology will also have applications for planetary exploration including studies of the Martian ice caps and the icy moons of the outer solar system. Through the concept developed here, *we believe that we can image the base and map the 3-dimenional basal topography beneath an ice sheet at up to 5 km depth.*

This is the first annual report of the GISIR project. GISIR is a collaborative project between The Ohio State University, The Jet Propulsion Laboratory, The University of Kansas, Vexcel Corporation, E.G.&G, and Wallops Flight Facility.

2.0 GISIR Concept and Project Overview

GISIR is based on a novel interferometric filtering concept capable of overcoming the surface clutter problems and enabling two-dimensional swath mapping of the polar regions in a short duration mission. The idea behind interferometric filtering for clutter reduction is based on the fact that scattering from ice sheets consists of three components: a) ice-air interface and near surface density variations; b) ice-bed interface; and c) intermediate layers, due mainly to changes in conductivity. The intermediate layers are weakly scattering even in the specular direction (reflection coefficients of –60 to –80dB) and can be neglected at off-nadir incidence. Thus off-nadir scattering can be treated as resulting from two interfaces. Because the speckle from the two interfaces is not correlated, the average radar interferogram, a complex product between the two interferometric channels, can be modelled as the sum of the interferogram from the basal and surface layers. In the near-nadir direction, the basal fringes (which are due to scattering near nadir) will vary much faster with range (or cross-track distance) than fringes from the clutter (which is generated at larger angles). Consequently, band-limited filtering of the measured interferogram can be used to separate either the surface component of the basal component from the net signature. Basal layer slopes, and, to a lesser degree, ice sheet slopes, will modulate the fringe rate, but in the near nadir direction the main contribution to the fringe rate will be the flat surface term, and surface slopes only play a secondary role. Verifying that interferogram filtering can be successfully used to measure the bottom topography of ice sheets is a primary objective of the GISIR project.

In addition to evaluating the interferogram filtering concept for clutter rejection, the project will also investigate multibaseline tomography as an alternative clutter rejection scheme. This technique is likely to be practical from aircraft. Spaceborne implementation may be limited by unknown temporal rates of signal decorrelation.

The GISIR project is composed of 4 primary tasks. The first task, which is largely complete, is an analytic feasibility assessment. This work is discussed in two published papers and one which is in preparation (see section 7). The second task is to more rigorously test the concept by simulating synthetic aperture radar data over natural topographies and then applying the interferometric filtering and tomographic concepts to retrieve the ice thickness. Simulations are discussed in section 3. The third task is to build a P-band and VHF radar to be flown from aircraft over the Greenland Ice Sheet. Radar development is discussed in section 4. The fourth task is to use develop real time and post flight processors to reduce the radar and navigation data to swath reflectivity and ice thickness maps. This is primarily a year 2 objective but the topic is touched on in section 3. Additional tasks include flight planning, which includes selection of sights of interest to the science community, and sensitivity studies to determine the effect of water layers on the radar return.

3.0 GISIR Simulations

The purpose of this work is to evaluate the GISIR technique through simulations. The simulations also provide guidance about the space-borne and airborne SAR system design and data processing procedures.

The approach used for this analysis includes (1) simulation of phase history data using the geometry and characteristics planned for GISIR; (2) processing phase history data to single look complex data and interferograms using VEXCEL's space-borne and airborne SAR Processor and IFSAR processor; (3) performance assessment of clutter cancellation and mapping basal topography.

3.1 Radar Parameters

Simulation parameters are listed in Tables 3.1.1 and 3.1.2.

Table 3.1.1 Space-borne simulation parameters

PARAMETERS	P-BAND
RF Carrier Frequency (MHz)	430 MHz
RF Bandwidth (MHz)	6 MHz
Transmit Pulse Width (usec)	20 usec
PRF	1000 Hz
Sampling Frequency (MHz)	120
baseline	45 m

Table 3.1.2 Airborne simulation parameters

Characteristics	VHF	P-Band
RF Carrier Frequency (MHz)	150	450
RF Bandwidth (MHz)	20	50
Transmit Pulse Width (usec)	10 us	20 us
PRF (kHz)	0.001-10000	0.001-10000

Sampling Frequency (MHz)	120	120
Antenna Beam for airborne (4-elements)	22 degrees – cross track	22 degrees – cross track
Simulated baseline	20 m	20 m

3.2 Ice mass reflection and refraction modeling

The imaging geometry adopted for the simulations is shown in figure 3.1.

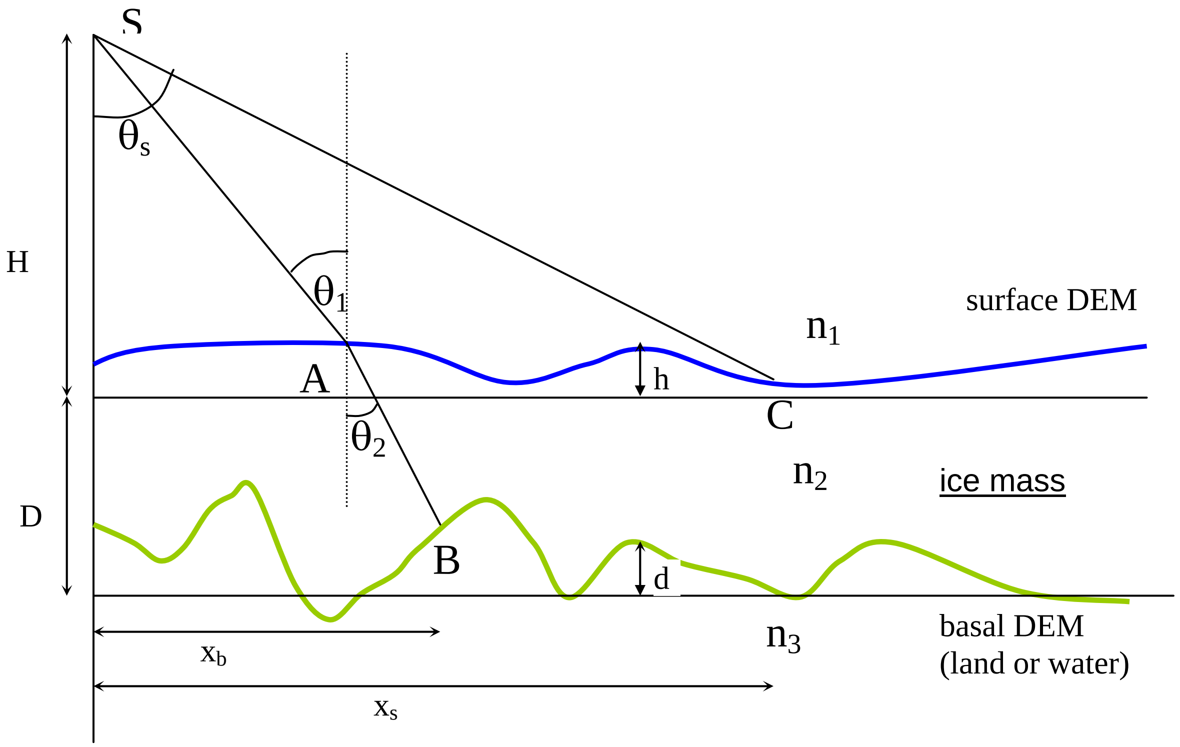

Fig. 3.1 ice mass reflection and refraction

Parameter definitions are:

n_1: refraction index for air ($n_1 \approx 1$)
n_2: refraction index for ice ($n_2 \approx 1.8$)
n_3: refraction index of land or seas water ($n_3 \approx 9$ for sea water, $n_3 \approx 5.5$ for wet land, $n_3 \approx 3$ for Greenland subglacial terrain)
v_1: speed of electromagnetic wave in air C ($\approx 3\text{x}10^8$ m/s)
v_2: speed of electromagnetic wave in ice ($\approx 3\text{x}10^8 / 1.8$ m/s)
Ice attenuation taken to be 0.9 dB per 100 m.

3.3 Phase History Simulation

Two independent steps are involved in the phase history simulation. The first step is to generate the reflectivity map of the scene according to the data acquisition geometry and the scattering properties of the scene. The received echo at the sensor for each pulse and each slant range bin is composed of surface and base contributions. The surface contribution comes from the backscattering of the transmitted signal at the air-ice interface. The basal contribution undergoes the refraction through the ice mass, backscattering on the boundary between the ice mass and the base, and the refraction from the ice mass back to the free air. The second step is to create the phase history raw data from the reflectivity map for both the receiving antennas using the inverse chirp scaling algorithm.

3.3.1 Generating the Reflectivity Map

The geometry is shown in Figure 3.2. To simplify the calculation, we implemented a ground range based algorithm.

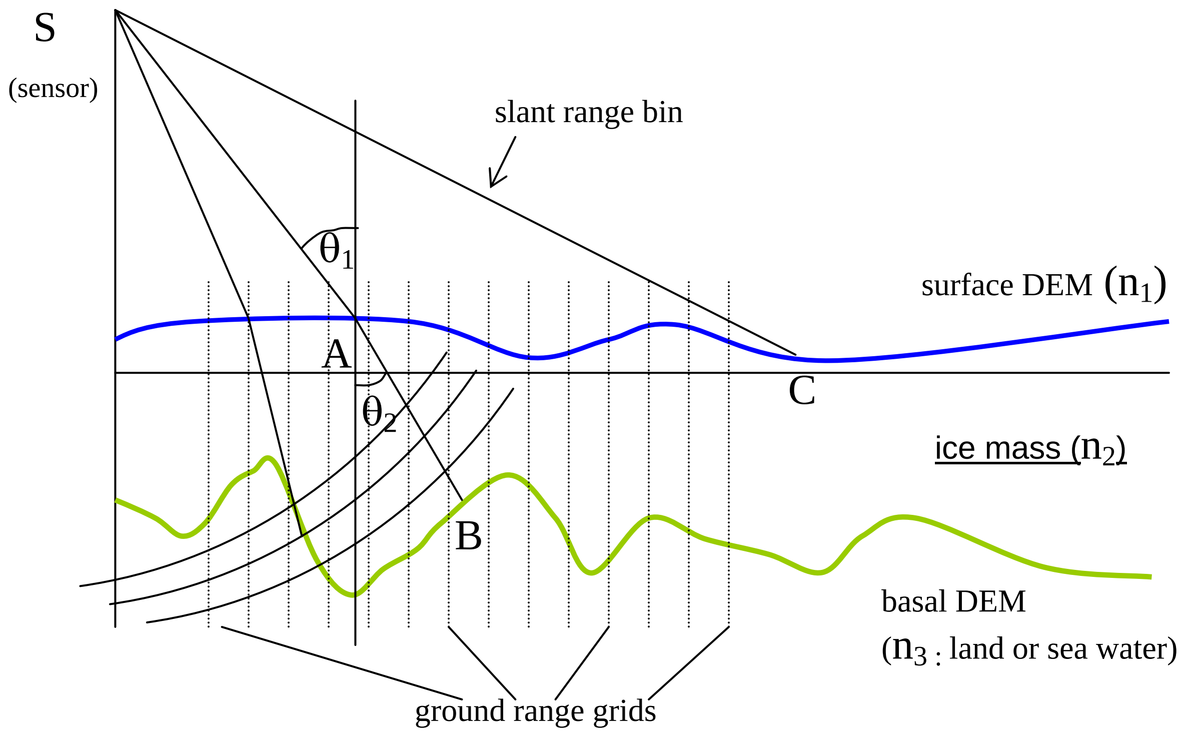

Fig. 3.2 Implementation of reflectivity map calculation

All quantities are calculated at each integer ground range grid point. These quantities include slant range, incidence angle, refraction angle and reflection coefficients for both surface and base. Any slant range grid point will lie somewhere between two neighboring ground range grid points. So, the reflectivity coefficient for each slant range grid point is calculated through interpolation between the two neighboring ground range bins. All the other quantities at each slant range grid point are calculated in this way.

When calculating the reflection from facets used to model the basal topography, we start from the ground range grid on the surface. At each surface ground range grid point, the basal reflection coefficient and the slant range from the sensor to the basal grid point are calculated. Bilinear interpolation is used to assure that each basal grid point is sampled.

For the second orbit necessary for repeat pass interferometry or multibaseline tomography, 4 more parameters are needed to setup a baseline and to specify temporal decorrelation. At this point, we do not include temporal decorrleation in the analysis. All the calculations for the second orbit are the same as for the reference orbit except the interferometric phase, which is the result of the non-zero baseline and topography.

3.3.2 Generating phase history data

Using the range information computed above, the inverse chirp scaling algorithm is implemented to convert the reflectivity maps to phase history data for the two antenna interferometer. The same approach is used for repeat pass reference and secondary orbits.

3.4 Airborne SAR Simulator

Vexcel's Scatter is a space-borne SAR phase history simulator. To simulate an airborne SAR system we made the following changes:

- add airborne platform navigation parameters
- ability to simulate air turbulence
- included more than one slave antennas

3.4.1 Generate airborne sensor track

The following scene and platform parameters are used to generate a straight line track:

- Scene center : $S_C(\lambda, \theta, 0)$
- Altitude : h
- Track angle : α
- Left or right looking
- Look angle : θ_L

An initial, straight line track is represented by the Peg point, which is the reference point of the platform in space, the $\vec{Peg}$ is vector, which connects the center of the earth to the reference point, and the heading vector $\vec{V}$. The Peg point and the heading can be determined by using the scene and platform parameters shown above and with the help of Fig, 3.3

3.4.2 Air turbulence simulation

The actual track of the sensor is composed of three portions: straight line track determined by Peg and sensor Heading, known track position deviation from the straight line and unknown track position error. Both the known track position deviation and the unknown error are described by sinusoid functions as follows:

Along Track: $\Delta x = \Delta x_d \cdot \sin(2\pi f_{xd} t + \Psi_{xd}) + \Delta x_e \cdot \sin(2\pi f_{xe} t + \Psi_{xe})$,

Horizontal: $\Delta y = \Delta y_d \cdot \sin(2\pi f_{yd} t + \Psi_{yd}) + \Delta y_e \cdot \sin(2\pi f_{ye} t + \Psi_{ye})$,

Vertical: $\Delta z = \Delta z_d \cdot \sin(2\pi f_{zd} t + \Psi_{zd}) + \Delta y_e \cdot \sin(2\pi f_{ze} t + \Psi_{ze})$,

where x, y and z represent along track, horizontal and vertical direction, respectively. The subscript d represents known track position deviation and the subscript e represents the unknown track position error.

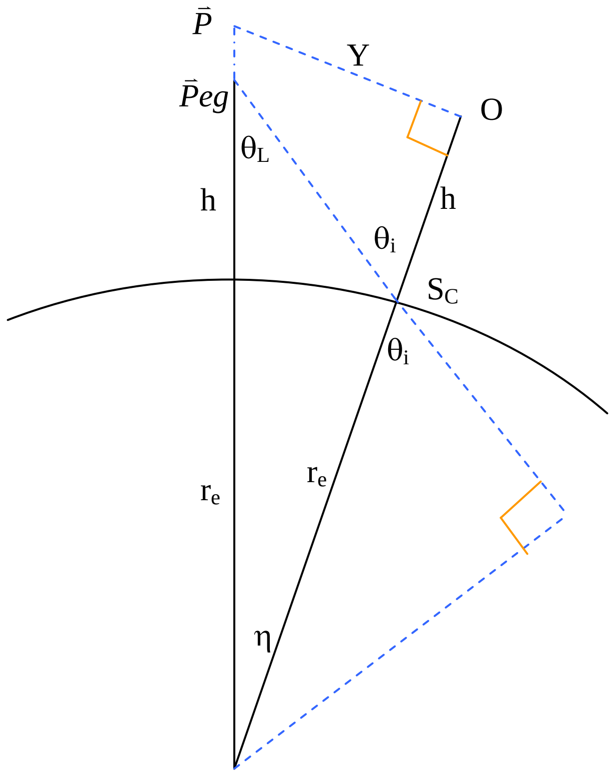

Fig. 3.3 Determining Peg and heading of an airborne straight line track.

3.4.3 Multiple slave antennas simulation

The GISIR airborne radar could carry 8 or more dipole antenna elements, some of which transmit and some or all receive. We modified Scatter so that it now supports multiple slave antennas simulation.

Four parameters are required to specify the constant baseline and temporal decorrelation between each slave antenna and the reference antenna. They are: along track baseline component, parallel baseline component, perpendicular baseline component and the temporal decorrelation.

3.5 Airborne SAR processor description

We implemented the convolution back-projection (CBP) algorithm and the fast back-projection (FBP) algorithm to process the simulated airborne GISIR data.

3.5.1 CBP – convolution back-projection algorithm

The radar sensor transmits a chirp pulse signal:

$$s(t)=\begin{cases} e^{j2\pi\left(f_0 t+\frac{1}{2}\gamma t^2\right)}, & |t|<\dfrac{T}{2} \\ 0, & otherwise \end{cases} \tag{1}$$

The returned square wave modulated signal from a scatterer at a distance R to the sensor after deramp processing is:

$$s_0(n,\hat{t})=rect\left(\frac{\hat{t}-2\frac{R_t}{c}}{T}\right)\cdot e^{j\Phi(n,\hat{t})} \tag{2}$$

with

$$\Phi(n,\hat{t})=-\frac{4\pi\gamma}{c}\left(\frac{f_c}{\gamma}+\hat{t}-\frac{2R_a}{c}\right)\cdot(R_t-R_a)+\frac{4\pi\gamma}{c^2}\cdot(R_t-R_a)^2 \tag{3}$$

and

$$\hat{t}=t-mT\ ,$$

where T is the pulse repetition interval.

After range compression, i.e., Fourier transform with respect to the fast time t, the range compressed data can be expressed as:

$$S(n,f)=\sin c\left(\pi T\left(f-\frac{2\gamma R_\Delta}{c}\right)\right)\cdot\exp\left\{j\left[\frac{4\pi(f-f_c)}{c}R_\Delta-\frac{4\pi\gamma}{c^2}R_\Delta^2\right]\right\} \tag{4}$$

To compensate the quadratic phase term in (4) range deskew processing is applied to (4) after range compression by multiplying the range compressed data with a phase factor of $\exp\{-j\pi f^2/\gamma\}$. The resulted data from the range deskew processing will be:

$$S(n,f)=\sin c\left(\pi T\left(f-\frac{2\gamma R_\Delta}{c}\right)\right)\cdot\exp\left\{-j\frac{4\pi R_\Delta}{\lambda}\right\} \tag{5}$$

(5) is a projection available for image formation. Along the aperture there are altogether N projections from each of N pulses.

The back projection algorithm projects the received pulse data back to the scatterer position on the surface and accumulates the back projected data for all the pulses. Mathematically for an image point(i, j), the image(i, j) formed from back projection can be expressed as :

$$image(i,j)=\sum_{n=0}^{N-1}S\left(n,\frac{2\gamma}{c}r_{ij}(n)\right)\cdot\exp\left\{j\frac{4\pi}{\lambda}\left[r_{ij}(n)-R_a\right]\right\} \tag{6}$$

where $r_{ij}(n)$ is the range between the sensor and the image position at n-th pulse.

3.5.2 FBP – fast back projection algorithm

The fast back projection algorithm speeds up the calculation of (6) for the general SAR data acquisition geometry. The basis of this algorithm is that the required sampling rate to acquire the scene data is dependent on the size of the scene. If the scene to be imaged is small a larger sampling interval can be used *without causing an ambiguity*. On the other hand for a large scene a smaller sampling interval is necessary to avoid ambiguities in the range and azimuth directions.

We implemented the Fast Back Projection (FBP) presented in “L.M.H Ulander, H. Hellsten and G. Senstroem : Synthetic aperture radar processing using fast factored back-projection, IEEE Trans. Aerosp. Electr. Sys., v.39, pp 760-776, 2003”. It divides the direct back-projection process into stages (figure 3.4). In each stage, a set of approximate down sampled versions of the SAR aperture, each valid over a portion of the scene, is processed to form a more coarsely sampled set of apertures valid on smaller portions of the scene.

FBP reduced the computational cost of CBP. This computational advantage causes some low magnitude artifacts, which are the results of accumulated interpolation error. For very high contrast scenes the artifacts could be significant. The following flow chart shows how the FBP processor is implemented.

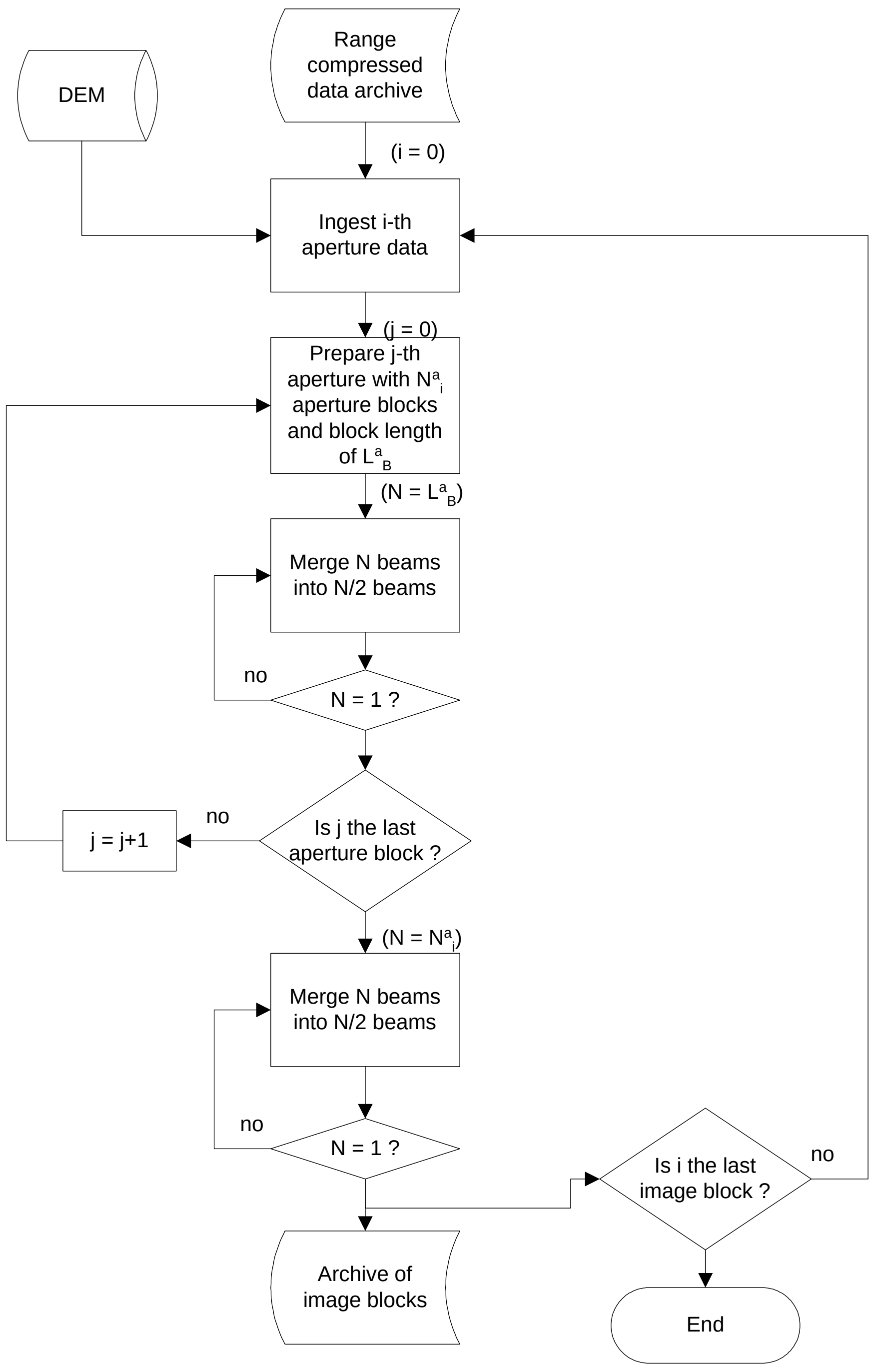

* Assume the processed image is divided into one or more image blocks.

* For i-th image block, calculate the i-th corresponding aperture A_i, which can be divided into N_i^a aperture blocks with block length $L_B^a = 2^K$.

* N is the variable for the number of beams.

Fig. 3.4 Flow chart of the fast back-projection algorithm.

3.6 Airborne IFSAR processor

Vexcel's current interferometric processor PHASE supports only space borne SAR data processing. We modified PHASE so that it can process data from Vexcel's airborne SAR processor and generate interferograms and do interferogram filtering and phase unwrapping.

3.7 Processing simulated Ice sounding radar data

3.7.1 Basic Relationships

Assume the two antennas are located at x = $\pm\frac{B}{2}$ on the ground range axis and each antenna transmits and receives separately. The distance between the sensor and a point on the surface can be described as :

$$r_s = H - h + \frac{x_s^2}{2 \cdot (H - h)} \tag{7}$$

and the interferometric phase of the point can be written as :

$$\Phi_s = 2kB\theta_s = 2kB\sqrt{\frac{2(r_s - H + h)}{H}} \tag{8}$$

where H is the orbit altitude, h is the elevation of the point on the surface, x is the ground range of the point, k = $\frac{2\pi}{\lambda}$ and Φ_s is the surface interferometric phase. Figure 1 defines parameters of H, D, h, d, θ_1, θ_2 and θ_S.

Similar equations can be derived for the basal surface:

$$r_b = H + n \cdot (D - d) + \tfrac{1}{2} \cdot \frac{x_b^2}{H + \frac{D - d}{n}} \tag{9}$$

and

$$\Phi_b = 2kB\theta_1 = 2kB\sqrt{\frac{2(r_s - H + h - n \cdot (D - d))}{H + \frac{D - d}{n}}} \tag{10}$$

where D is the global ice thickness and d is the basal elevation above D, θ_1 is the incidence angle from sensor to the upper surface and Φ_b is the basal interferometric phase.

If two points on the upper surface and on the basal meet the relationship:

$$x_s^2 = 2Hn(D-d) + \frac{x_b^2}{1+\frac{D-d}{nH}} \tag{11}$$

or

$$x_b^2 = (1+\frac{D-d}{nH})\cdot(x_s^2 - 2Hn(D-d)) \tag{12}$$

they will be in the same range bin.

3.7.2 Extract surface DEM

We band pass filter the interferogram to retrieve the phase data associated with the surface. The fractional phase value we measure from the filtered interferogram has an undetermined phase offset Φ_{sc}. If we use $\hat{\Phi}_s$ to represent the measured phase value at each azimuth position and range bin we have

$$\Phi_s = \hat{\Phi}_s + \Phi_{sc} = 2kB\sqrt{\frac{2(r_s - H + h)}{H}} \tag{13}$$

If one ground control point is available we can use it to estimate the constant phase offset Φ_{sc}. If more control points are available the baseline B can be refined.

With refined baseline B and the estimated phase offset Φ_{sc} we can easily derive surface elevation for each point:

$$h = \frac{H\cdot(\hat{\Phi}_s + \Phi_{sc})^2}{2(2kB)^2} - (r_s - H) \tag{14}$$

3.7.3 Extract ice thickness

Conversely from section 3.7.2, we can filter the interferogram to retrieve the basal signature. We can unwrap the phase and make the phase measurements $\hat{\Phi}_b$. If all the basal phase is measurable starting from nadir, where the look angle θ_1 is zero, we do not need any other ground truth to determine unknown parameters. Practically speaking, we still need control points away from nadir because the basal phase changes rapidly near-nadir. To determine the phase offset Φ_{bc} we need at least one control point and using the relationship below:

$$\hat{\Phi}_b + \Phi_{bc} = 2kB\sqrt{\frac{2(r_s - H + h - n\cdot(D-d))}{H + \frac{D-d}{n}}} \tag{15}$$

After the phase offset Φ_{bc} is determined, the ice thickness can be derived from:

$$D - d = \frac{2\cdot(r_s - H + h) - H\cdot\left(\frac{\hat{\Phi}_b + \Phi_{bc}}{2kB}\right)^2}{2\cdot n + \frac{1}{n}\cdot\left(\frac{\hat{\Phi}_b + \Phi_{bc}}{2kB}\right)^2} \tag{16}$$

3.7.4 Clutter rejection – band-limit filtering

The precondition to be able to extract the basal interferometric phase and to derive the ice thickness using the interferometric sounding technology is the separation of the basal interferogram from the surface interferogram. The following two steps are developed to fulfill the task:

1) Apply the Goldstein filter to the mixed interferogram and Fourier transform the Goldstein filtered interferogram to determine the spatial frequencies of the interferogram.

2) A frequency-domain band-limit filter is applied to the original mixed interferogram by setting the spatial frequency components of the surface interferogram to zero. The procedure begins with a FFT of the interferogram in the range direction. The FFT length can be chosen according to the separation of the basal and surface interferogram. To reduce the boundary effect of the frequency-domain method a 50% overlap with triangular weighting is used. Multi-looking process is applied to the band-limit filtered full resolution interferogram to increase the SNR of the basal interferogram. Because the basal return is very weak compared with the surface return up to 100 azimuth looks should be used depending on the ice thickness.

3.8 Simulation results and analysis

3.8.1 P-band space-borne simulation and analysis

To investigate the interferometric technique under more complex situations, we did a phase history simulation based on the system parameters summarized in Table 3.2.1 and with a PRF of 2000 Hz. For the scene we selected a region in Greenland, where both coarse surface and base digital elevation models (DEMs) are available from the National Snow and Ice Data Center. The original DEMs including have posting spacing of 5 km, so we did 1/32 sinc interpolation to bring down the spacing to 156 m. Fig 3.5 shows the interpolated DEMs for the surface and the base. The corresponding DEMs in slant range geometry with ascending orbits are shown in Fig. 3.6.

The ice mass is assumed to lie on rock with a permittivity of 9. The permittivity of ice is taken as 3.24. A two-layer scene model is adopted. One boundary is the top interface between the free air and the ice mass and the other is the bottom interface between the ice and the basal rocks. The attenuation within the ice mass is assumed to be 9 dB per one kilometer. The thickness of the ice mass varies from about 2000 to 2540 meters depending on the location. The average ice thickness is about 2270 meters for the whole scene. The sensor, right looking, was assumed to fly on an ascending orbit from south to north with an orbit inclination angle of 85 degrees.

We then use VEXCEL's range-Doppler SAR processor to process the raw data to single look complex (SLC) data and use VEXCEL's InSAR processor to create the interferogram, which is shown in Fig. 3.7 after it is flattened. The interferogram is multi-looked with 80 looks in azimuth direction and has both surface and basal contributions. The surface contribution of the flattened interferogram has zero fringes and the basal contribution has a few fringes from the near to far range due to the smaller incidence angle on the base. Fig. 3.8 shows the spectrum of the interferogram, where the x-axis is the frequency of the fringes per slant range meter. The peak at the zero-frequency represents the surface interferogram component and the other peaks at its right side are the result of the basal interferogram contribution. Through a band-pass filter we can extract the basal interferogram contribution from the mixed interferogram. Fig. 3.9 shows the band-pass filtered interferogram, which represents mainly the basal interferogram. The basal topography and the ice mass thickness can be then derived from it. Fig. 3.10 shows the true ice thickness map. Fig. 3.11 shows the ice thickness derived from both surface and basal interferogram. Fig. 3.12 shows the errors of the derived ice thickness map. The central part of the region shows small errors between 0 and 20 m. The right-center areas show the biggest errors, which are caused by the limitations in our band-pass filter and phase unwrapping schemes. The problems arise in this region from the fact that there is only minimal separation between the surface and basal topography spectra. This effect is expected from purely geometrical arguments, since as the incidence angle increases, the incidence angle for the surface and subsurface approach each other, and the fringe rates of the clutter and subsurface cannot be differentiated. This limitation restricts the swaths that can be achieved from space to be smaller than about 50 km. In practice, this is a small restriction, since complete polar coverage at 60 degrees latitude, can be achieved with fewer than 200 orbits leading to complete polar coverage approximately every 16 days.

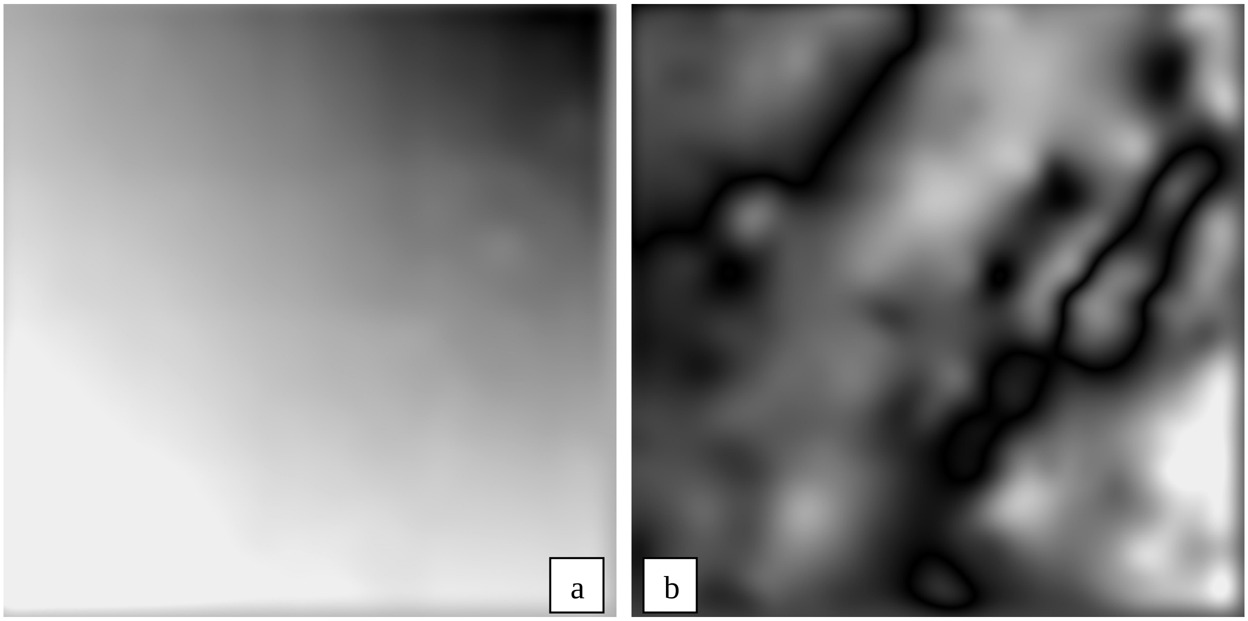

Fig. 3.5 (a) surface DEM and (b) basal DEM of a site in Greenland.

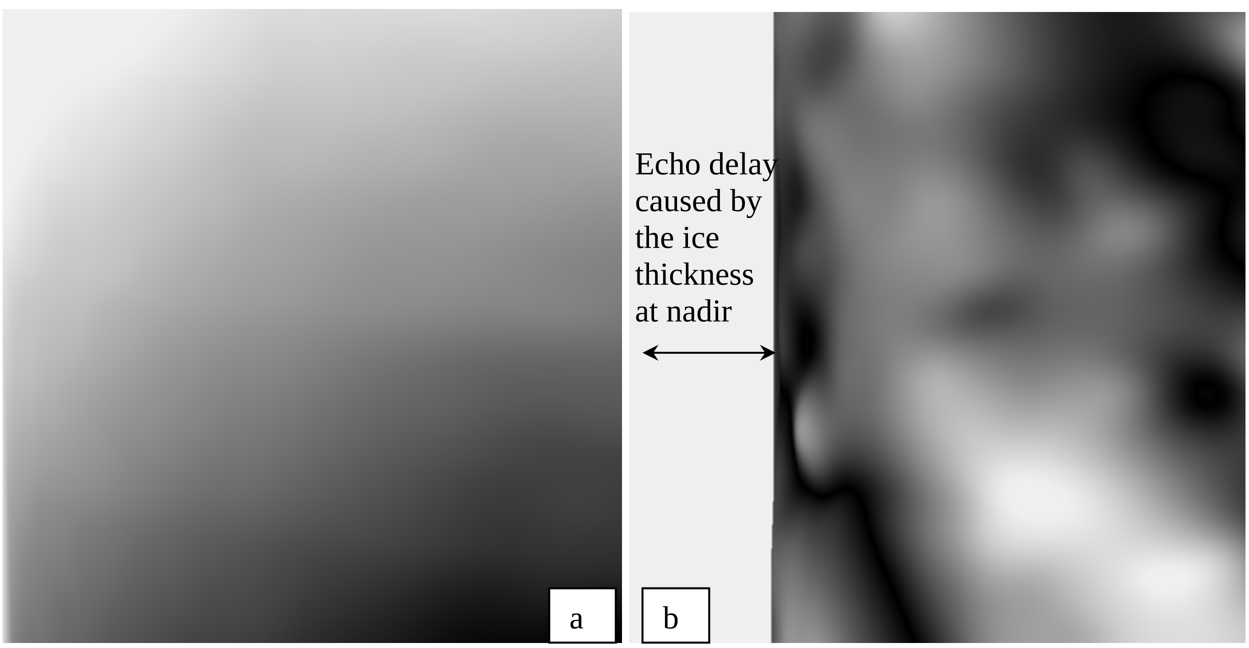

Fig. 3.6 (a) surface DEM and (b) basal DEM of a site in Greenland in slant range geometry with ascending orbits.

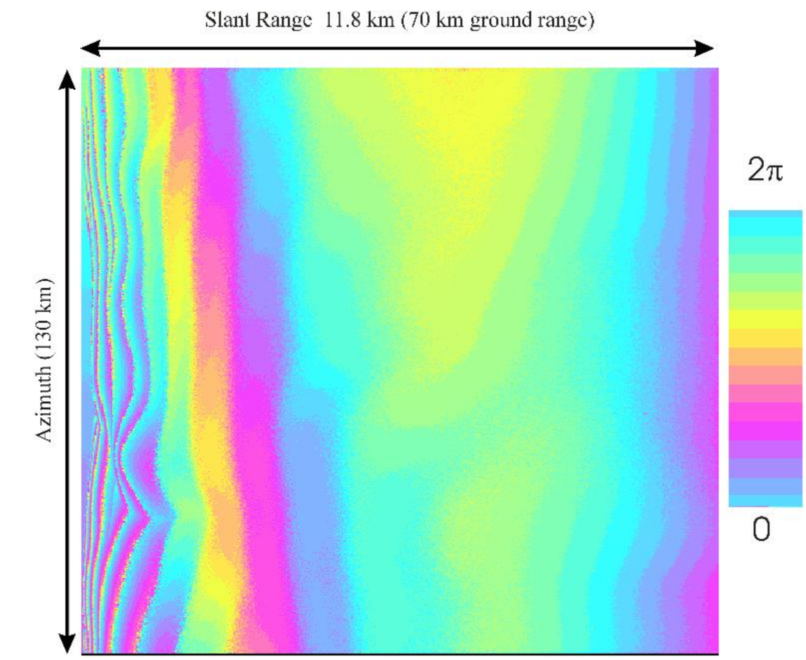

Figure 3.7. 1 by 50 looks *interferogram from processing simulated phase history data in a region of Greenland with average ice thickness of 2270 m. The interferogram was flattened with non-topography earth surface and is multi-looked with 80 azimuth looks.*

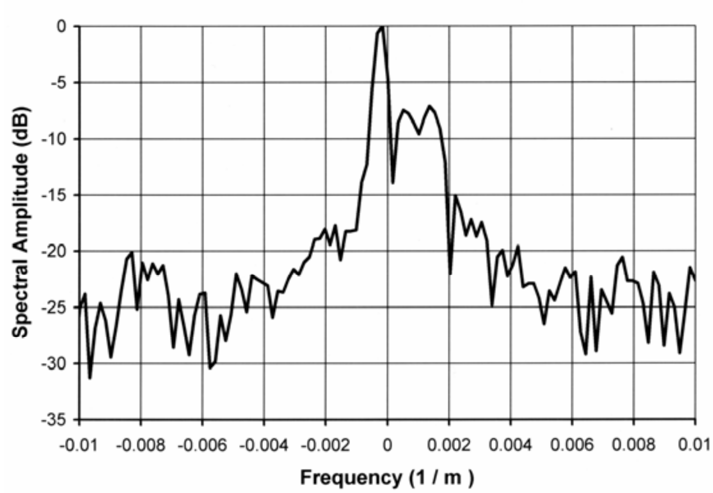

Figure 3.8. Spectrum of the interferogram in Fig. 7. The peak at 0 frequency represents the surface contribution and the peaks at the right side are from base contribution. The unit of the x-axis is number of fringes per slant range meter.

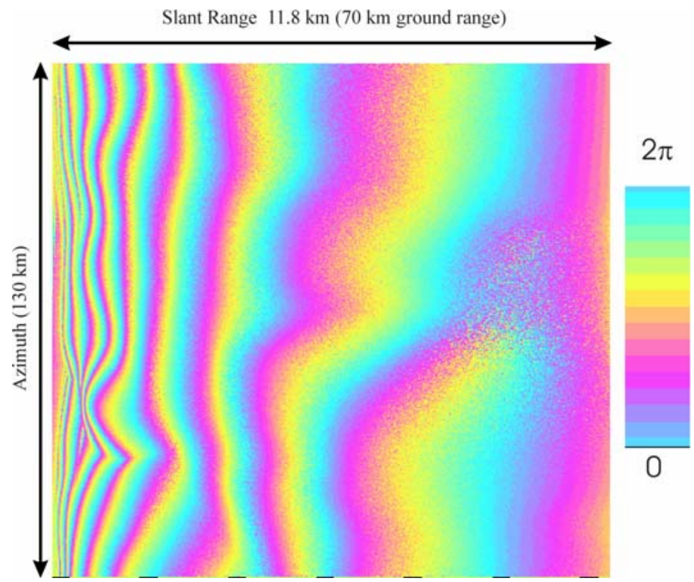

Figure 3.9. *Band-pass filtered interferogram filtered from Figure 7. It contains mainly the basal interferogram contribution, which can be used to derive basal topography and the ice mass thickness.*

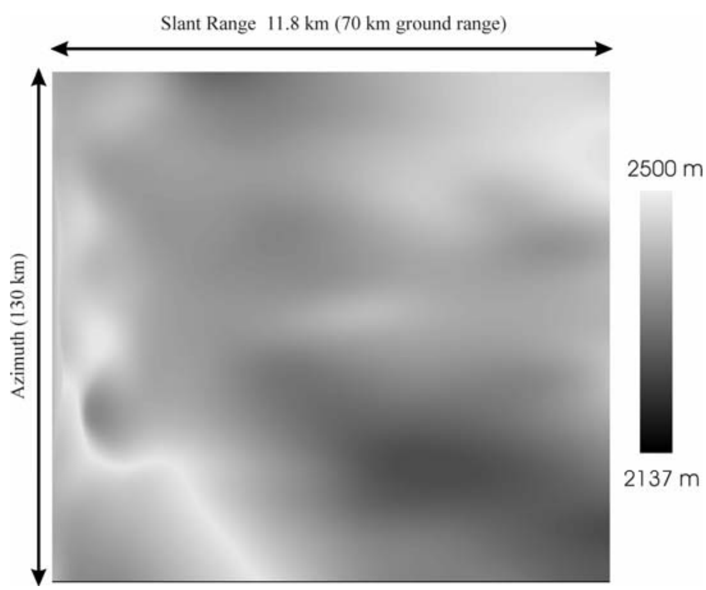

Figure 3.10. *Ice Thickness from the DEM.*

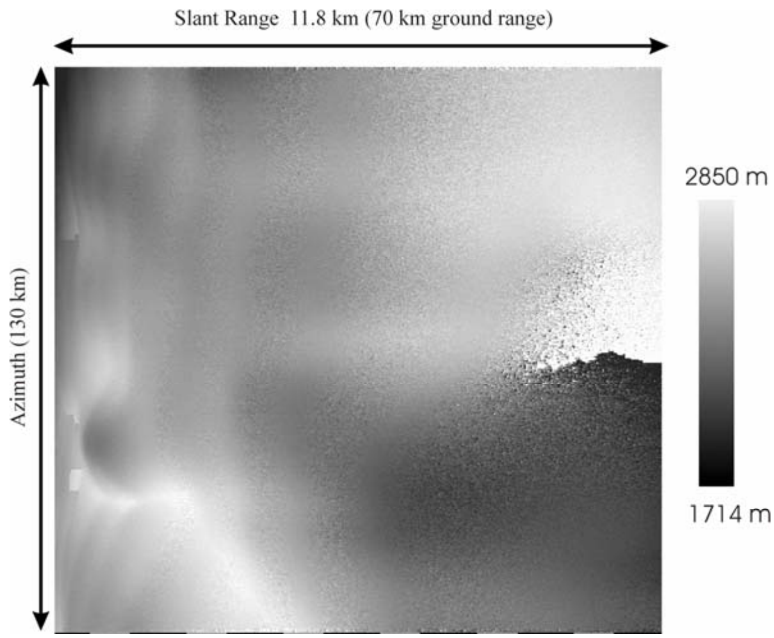

Figure 3.11. *Ice thickness derived from the interferogram.*

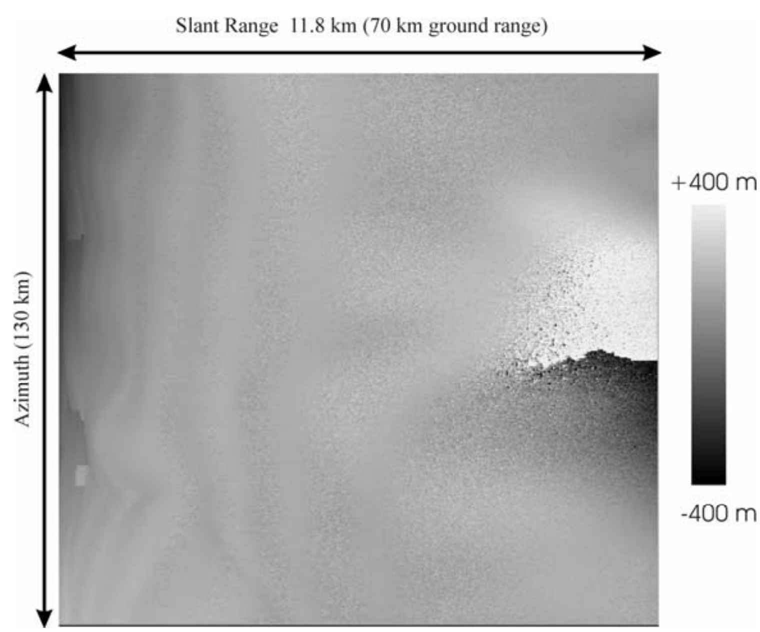

Figure 3.12. Ice thickness error map.

3.8.2 P-band airborne simulation and analysis

To investigate the interferometric clutter canceling technique for an airborne platform we did an airborne phase history simulation based on the system parameters summarized in Table 3.2. Again we selected a region in Greenland. The original DEMs including both surface and basal have posting spacing of 5 km we did a sinc interpolation to bring down the spacing to 31.25 m. Fig 3.13 shows the interpolated DEMs for the surface and the base. The thickness of the ice mass varies from about 800 to 850 meters.

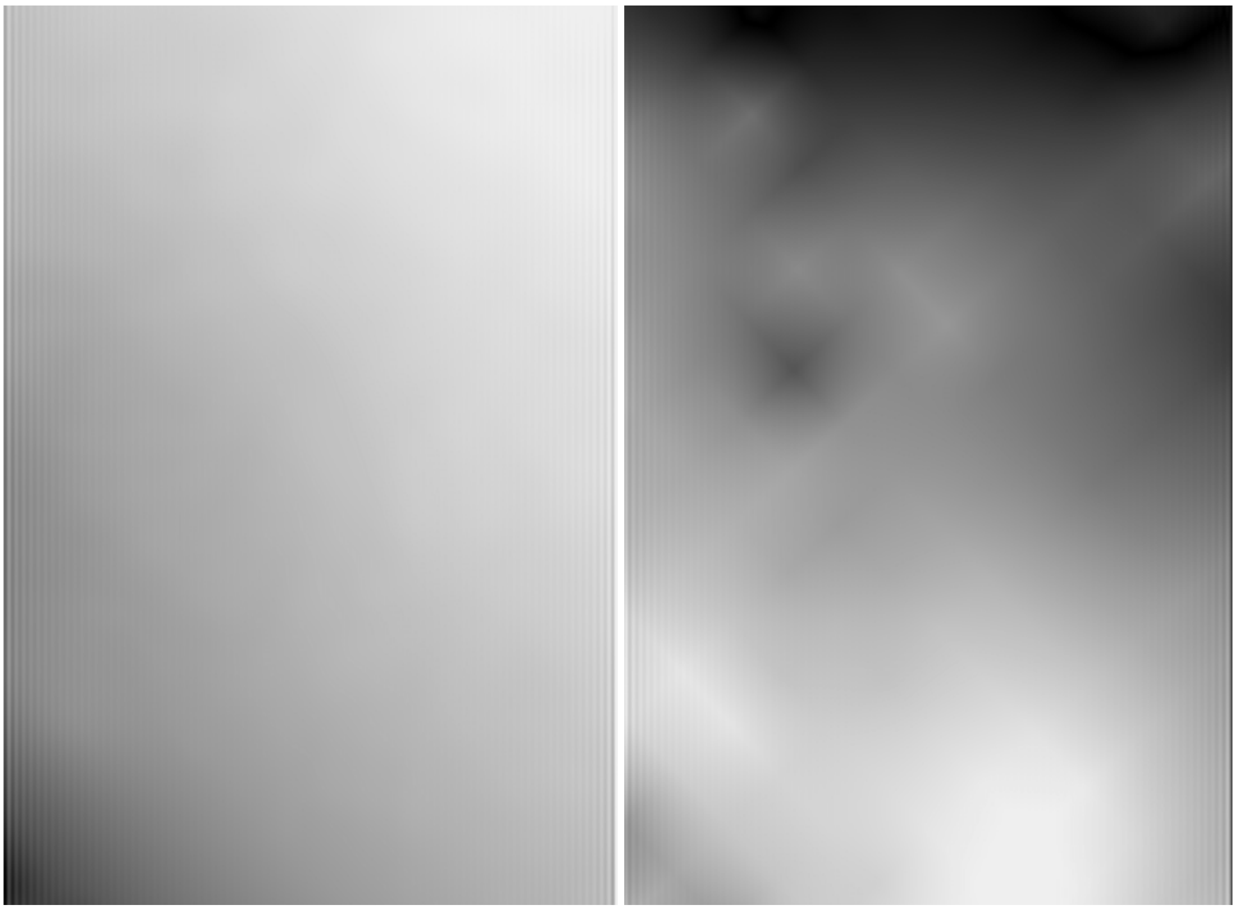

Fig. 3.13 Surface DEM (left) and Basal DEM (right).

The antenna patterns used for the simulation are shown in Fig. 3.14. The University of Kansas antenna system consists of 4 dipole elements, which are mounted under the wings of the aircraft.

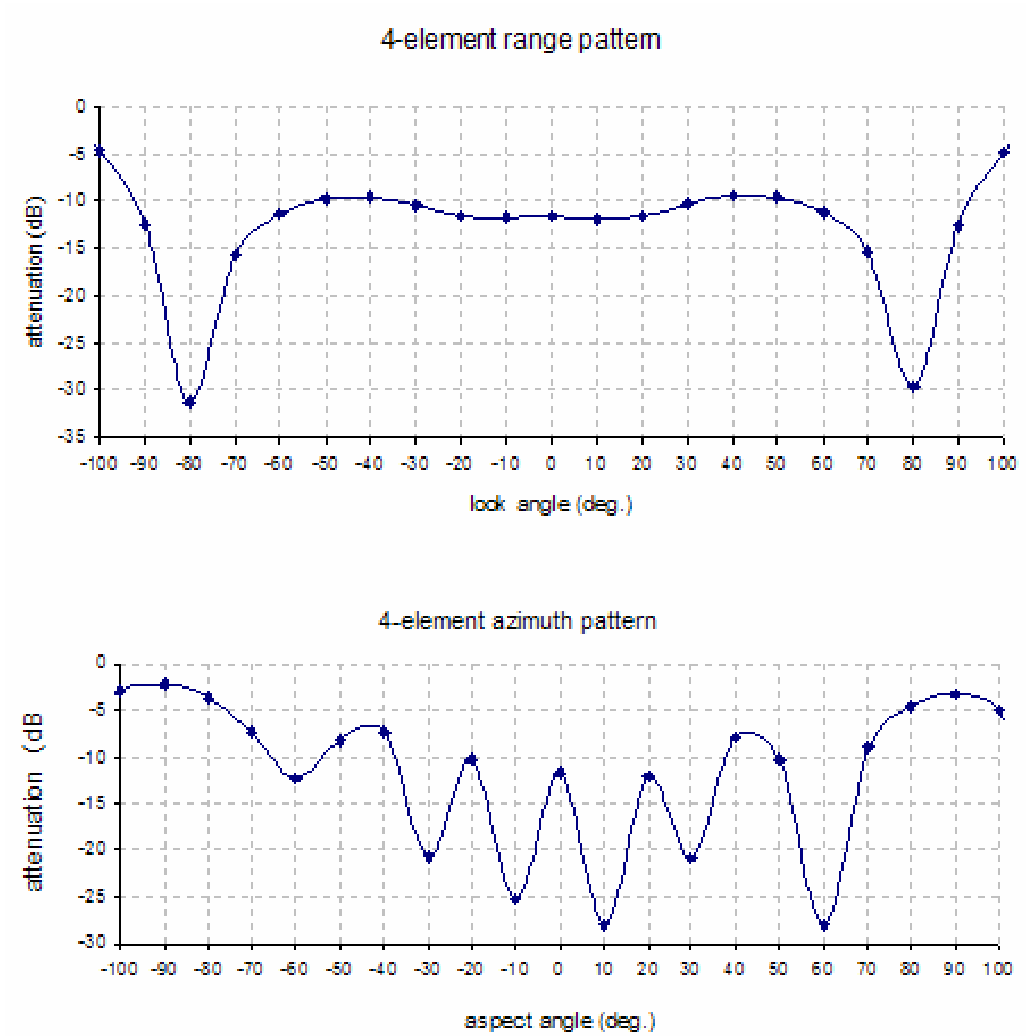

Fig. 3.14 Antenna patterns used for airborne simulation.

Fig. 3.15 shows (left) the reflectivity map of the scene, (center) the magnitude image of the simulated phase history data and (right) the processed SLC image using the fast back-projection algorithm. The mid-range, vertical bright lines in Fig. 3.15(left) and (right) are the results of the delayed basal returns due to the ice mass thickness.

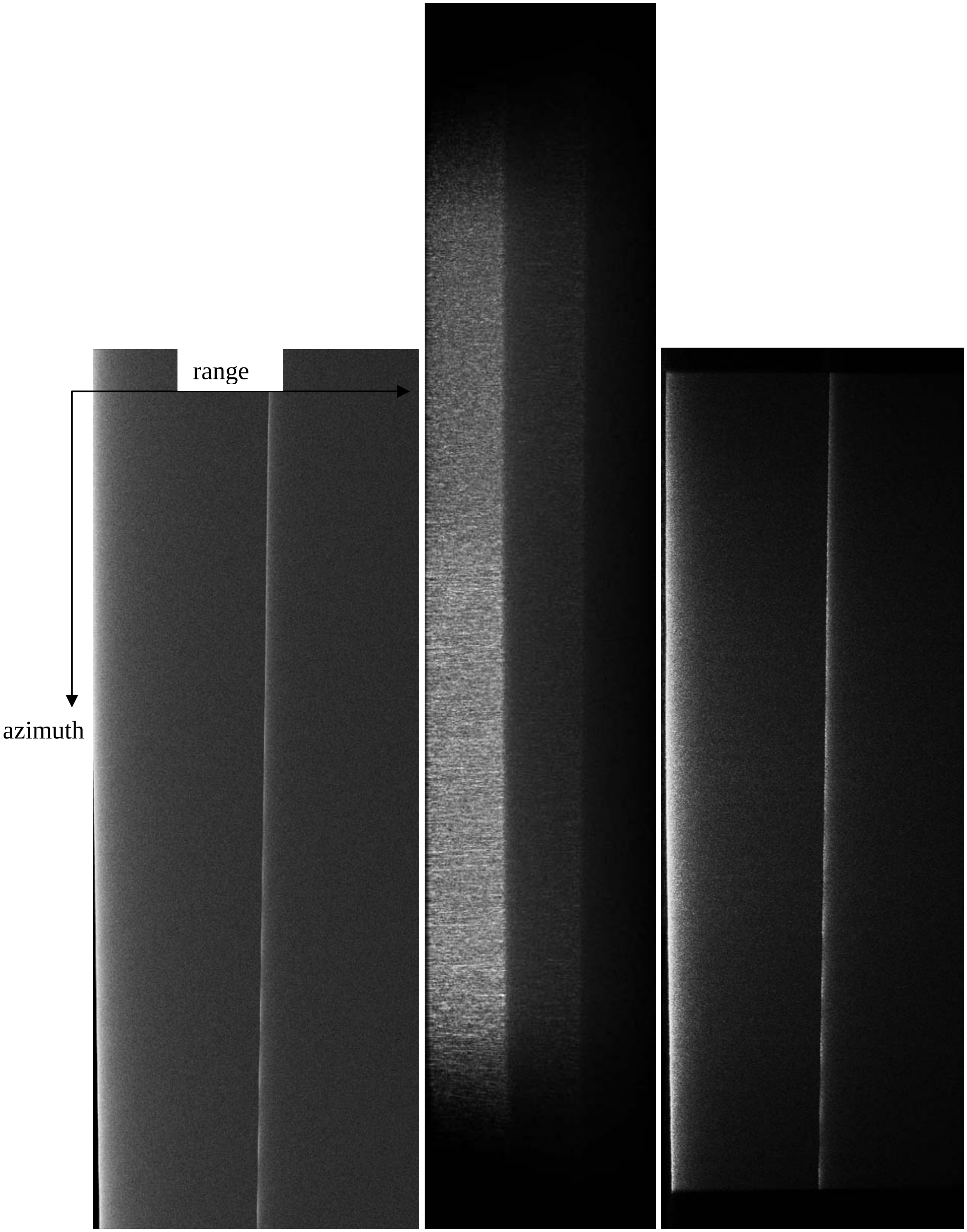

Fig. 3.15 ReflectivityMap (left), phase history data (middle) and processed SLC image (right).

Fig. 3.16 shows (top) the original interferogram with a 20 m baseline and 8 azimuth looks, and (milddle) the interferogram flattened with the ellipsoid earth surface and (bottom). The fringe rate is higher where the basal return begins to merge with the surface return.

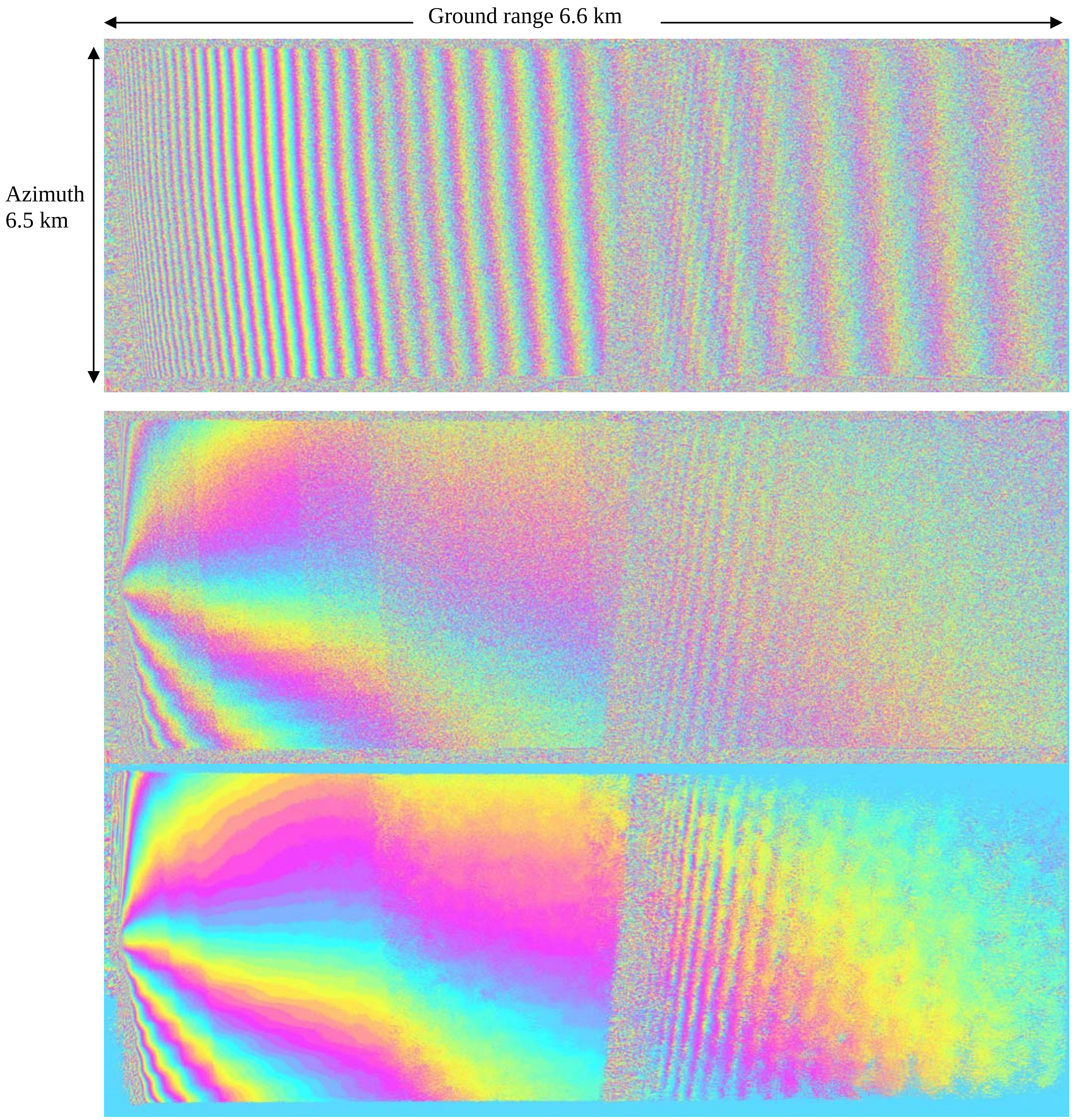

Fig. 3.16 (Top) Original interferograms with 8 azimuth looks, (middle) flattened interferogram and (bottom) Goldstein α–filter filtered interferogram.

We can derive the surface elevations from the interferogam shown in Fig. 3.16. Fig. 3.17 (top) shows the derived surface DEM. The block wise elevation errors in the middle range areas and the far range areas are caused by phase unwrapping process. Better phase unwrapping is needed for such interferograms with poor fringe quality. Fig. 3.17(bottom) is the elevation error map. The errors in the left part of the image are mostly within 10 meters.

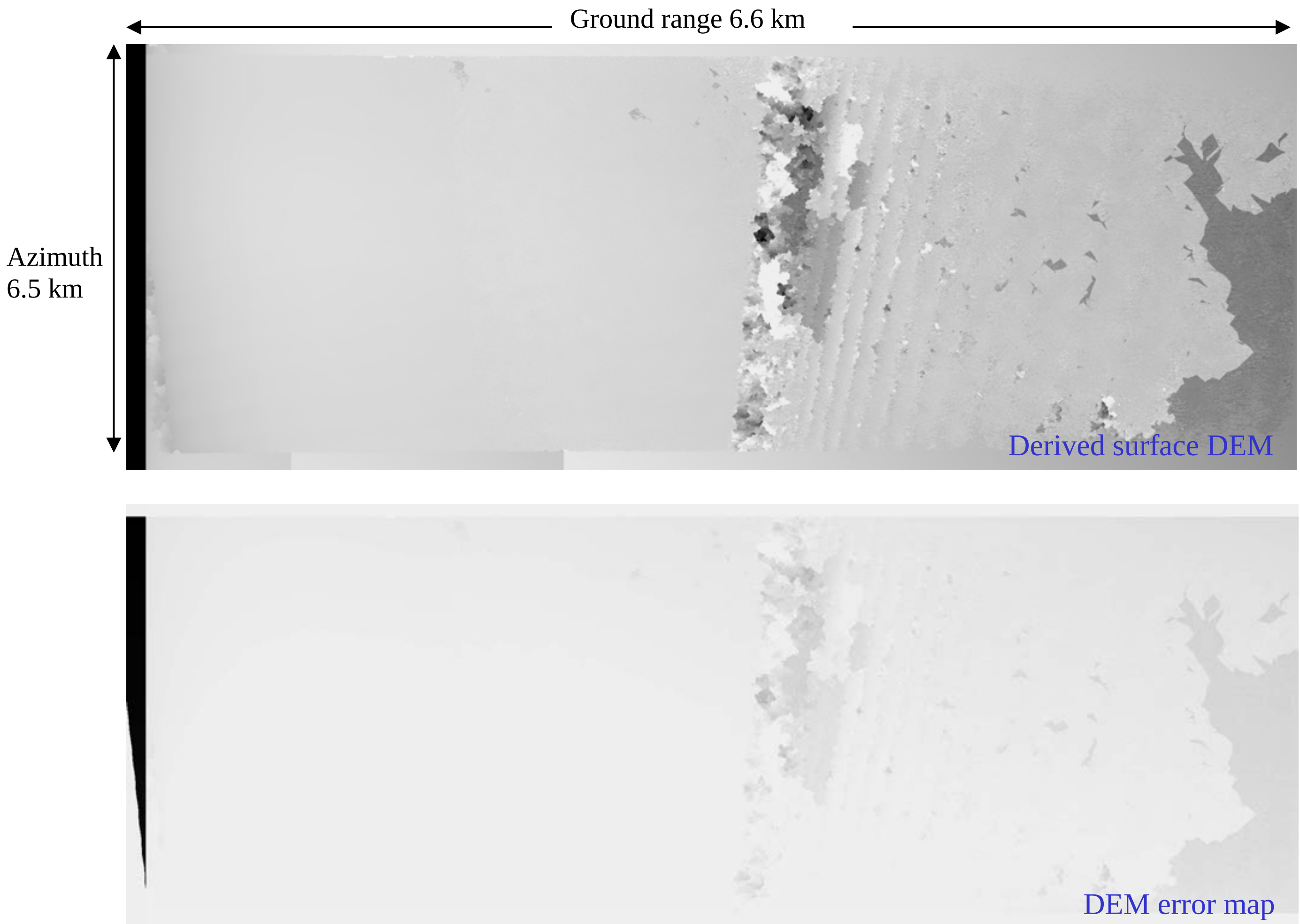

Fig. 3.17 Derived (upper) surface DEM and elevation error map (lower). The elevation error for the left part is mostly within 10 meters.

In order to extract the basal topography we need to extract the interferogram component of the base. Since the basal interferogram has a higher fringe rate the the surface return, we can do band-pass filtering on the mixed interferogram. Fig. 3.18 (a) is the original 8-looks mixed interferogram. Fig. 3.18(b) is the band-pass filtered interferorgam which contains mainly the basal component. Fig. 3.18(c) is Goldstein's α-Filtered result of Fig. 3.18(b). Fig. 3.18(d) is the unwrapped phase of Fig. 3.18(c).

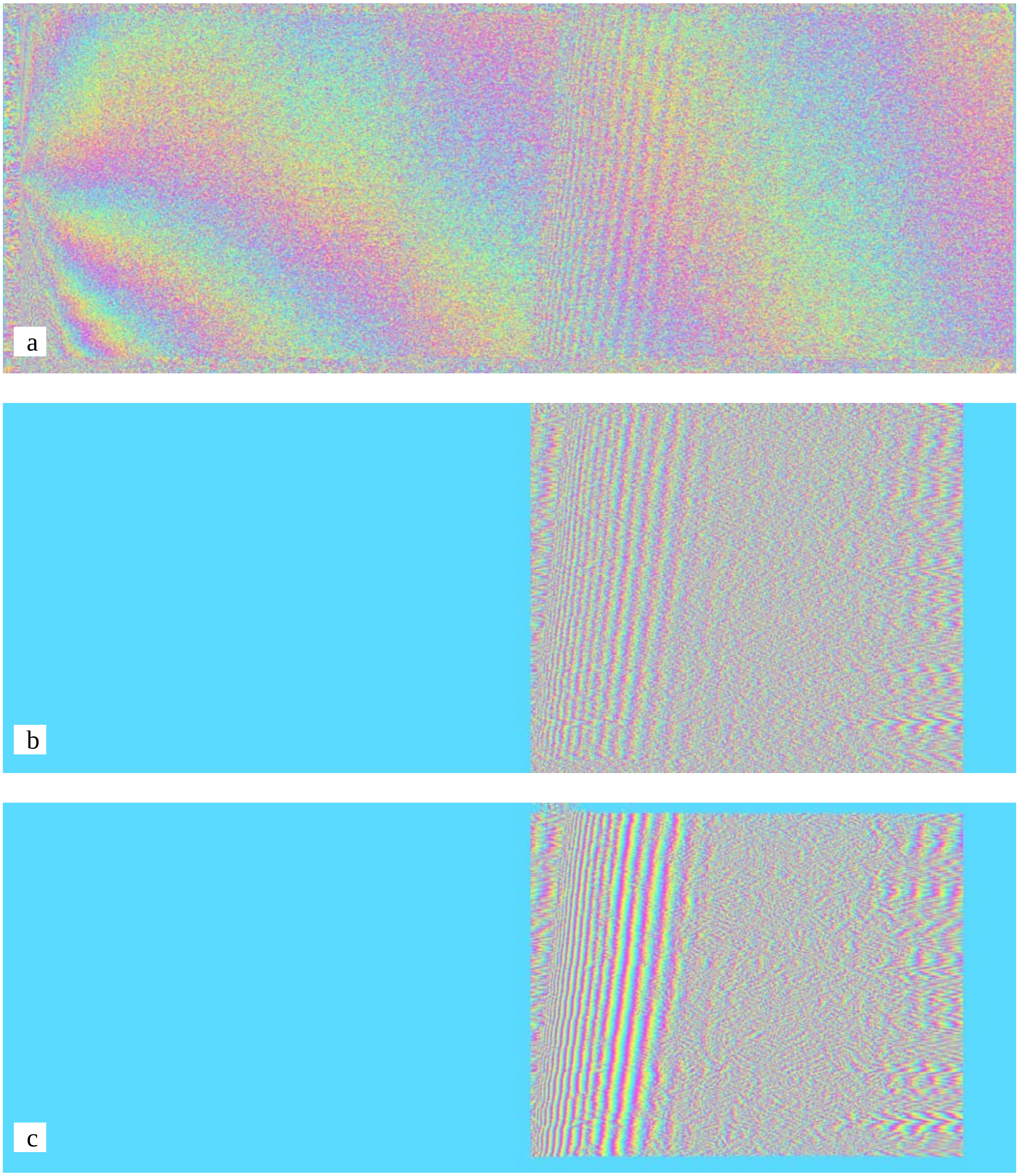
a
b
c

Fig. 3.18 (a) azimuth look interferogram, (b) band-pass filtered version, (c) after Goldstein α-Filtering and (d) unwrapped phase image.

3.8.3 VHF airborne simulation and analysis

We did a second airborne phase history simulation based on the VHF system parameters summarized in Table 2. The main differences between this simulation and the previous one in section 9.2 are the carrier frequency, RF signal bandwidth and the platform altitude. Fig. 3.19 shows (left) the reflectivity map of the scene, (center) the magnitude image of the simulated phase history data and (right) the processed SLC image using the fast back-projection algorithm. The vertical bright lines around the middle range in Fig. 3.19(left) and (right) are the results of the delayed basal returns due to the ice mass thickness.

Fig. 3.20 shows (upper) the 8-looks flattened interferogram, (middle) band-pass filtered interferorgam which contains mainly the basal component and (lower) Goldstein's α-Filtered result.

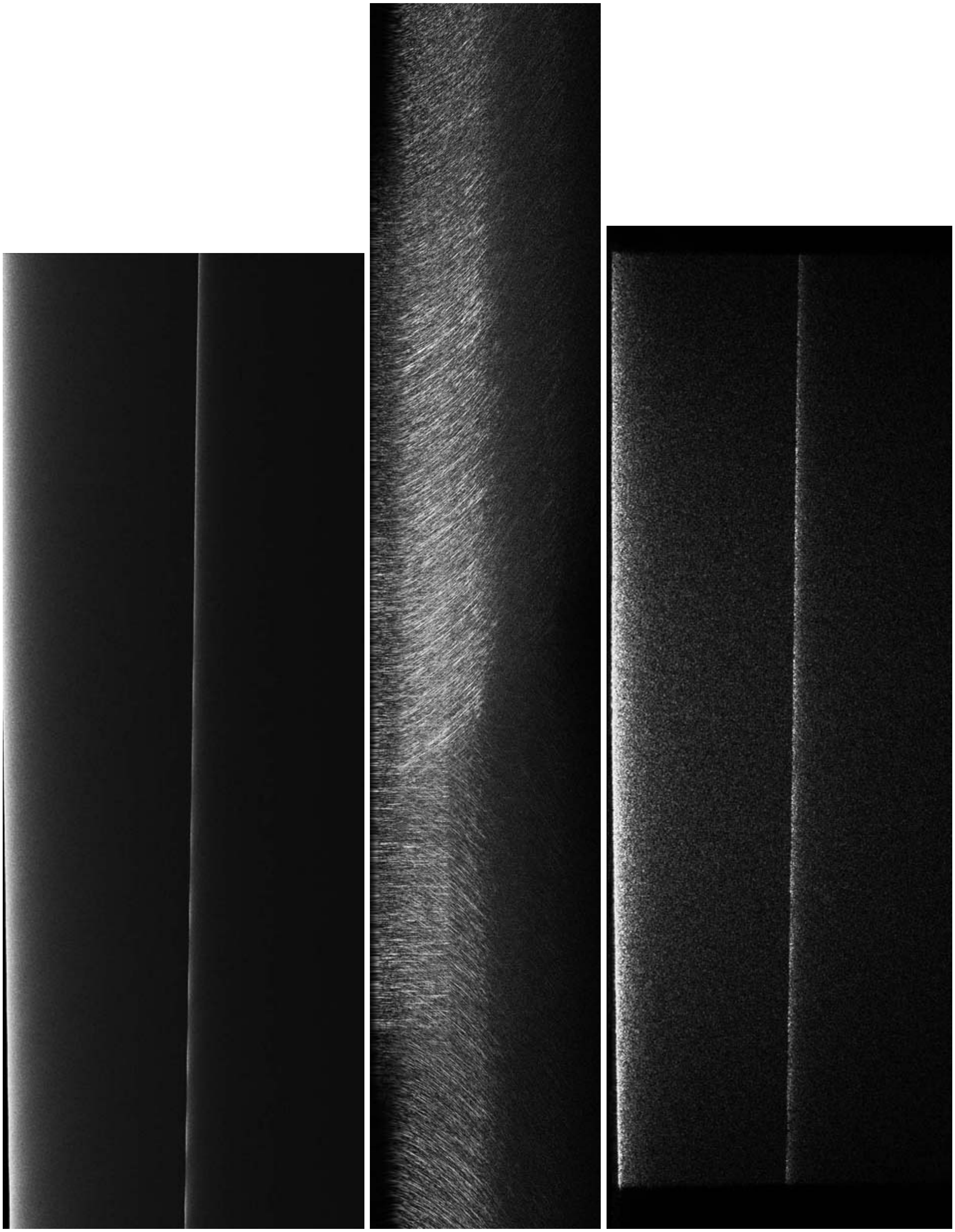

Fig. 3.19 ReflectivityMap (left), phase history data (middle) and processed SLC image (right).

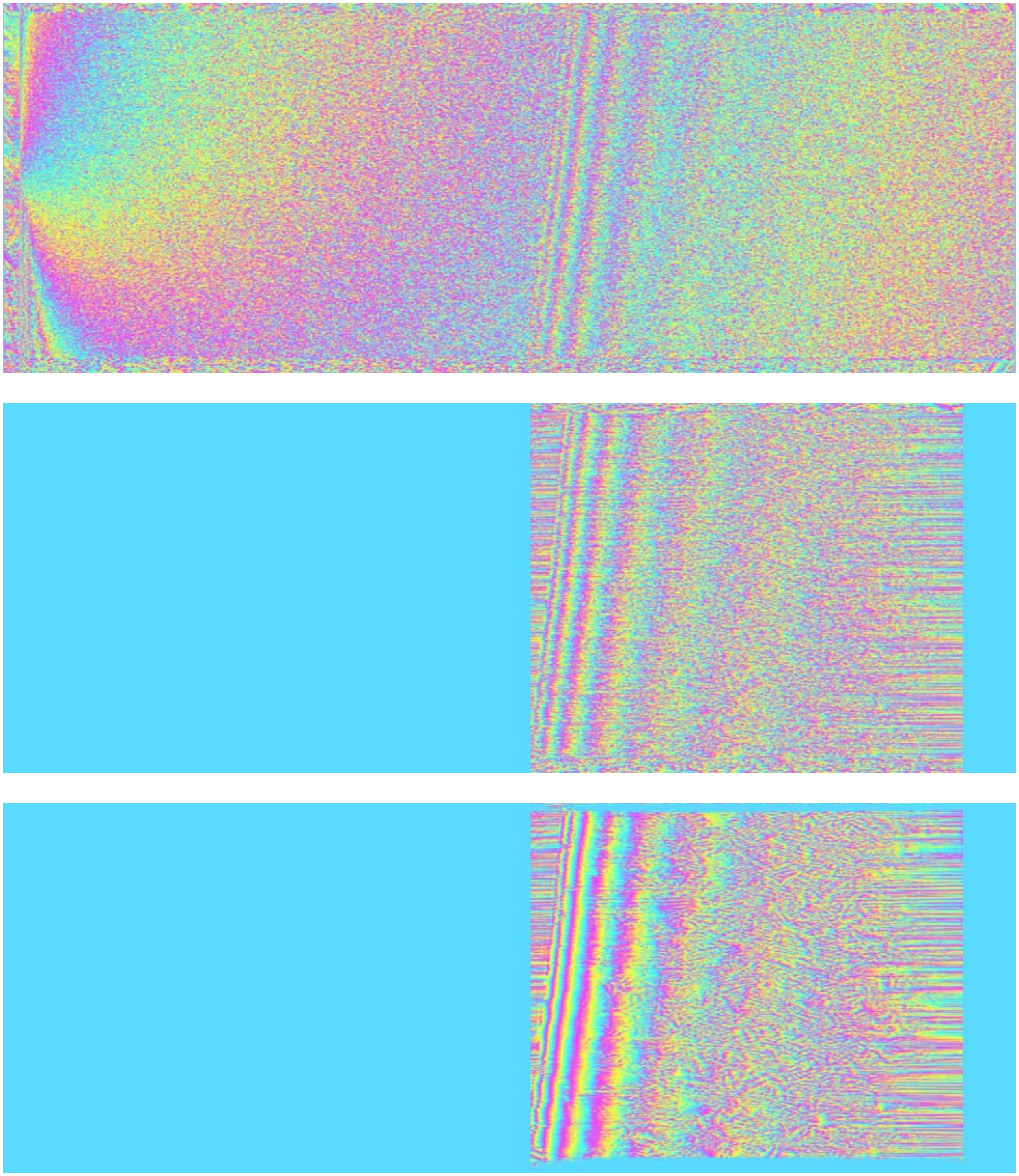

Fig. 3.20 VHF 8-look interferogram (upper), after band-pass filtering (middle) and after α–filtering (lower).

3.9 Discussion

The key to interferometric ice sounding technology is the separation of the basal interferogram contribution from the surface interferogram contribution. There are two factors affecting this separation.

The first one is the signal to clutter ratio (SCR), where the return from basal is considered as signal and the return from the surface is considered as clutter. For ice sounding case, the ice thickness and the contrast between the dielectric constants of ice and the bed will determine the SCR for a given wavelength. The SCR is acceptable in both P-band and VHF cases with about 800~900 meter ice thickness although 0.9 dB attenuation one-way per100 meter ice thickness is used. However we have yet to test the approach over very rough ice.

The second key factor affecting the separation is the interferogram fringe rate. At the same slant range bin the corresponding basal incidence angle is much smaller than that of the surface incidence angle assuming the surface and the basal are both pretty flat. Therefore by band-limit filtering we can extract the basal interferogram contribution from the mixed interferogram if the interferogram fringe rate has big enough separation between the basal and surface contributions. From the simulation results the fringe separation is big at near range areas for about 300m in ground range.

To further improve the quality of the basal interferogram and the results of ice mass thickness estimation, the following can be done:

- Time-domain band-pass filter to remove surface interferogram components
- Use more azimuth looks. Currently 8 azimuth looks are used
- Use a better phase unwrapping processor to improve the phase unwrapping results.

4.0 Radar Development

For its role in this project, the Center for Remote Sensing of Ice Sheets (CReSIS) is developing a radar that operates at 150 MHz with a bandwidth of 20 MHz and at 450 MHz with a bandwidth of 50MHz, and will collect data with a multi-phase-center antenna to test interferometric phase filtering and tomographic techniques to isolate returns from the ice bed and ice surface. The specific hardware tasks are as follows.

- Design, simulate, and build a radar with multiple receivers at 150 MHz and 450 MHz;
- Design and simulate the performance of an antenna array for collecting multi-phase center data;
- Develop and evaluate radar performance in the laboratory with simulated targets;
- Integrate radar and navigational systems on an aircraft.
- Conduct a field campaign to collect data;
- Process and distribute data;
- Analyze and synthesize results for presentation at conferences and publication in archival journals.

The specific tasks we addressed over the last ten months are as follows:

- Design of a new set of optimized antennas: We will in future build a model structure and measure its electrical performance.
- End-to-end simulation of the system, including antennas.
- Design of the radar.

In the following sections we provide a brief description of the system and progress made during the first three quarters of the first year.

4.1 Radar System Design

Figure 4.1.1 shows the system block diagram. It is modularized into four sub-systems: (1) radio frequency (RF) sub-system; (2) frequency synthesizer sub-system; (3) digital sub-system; and (4) antenna sub-system

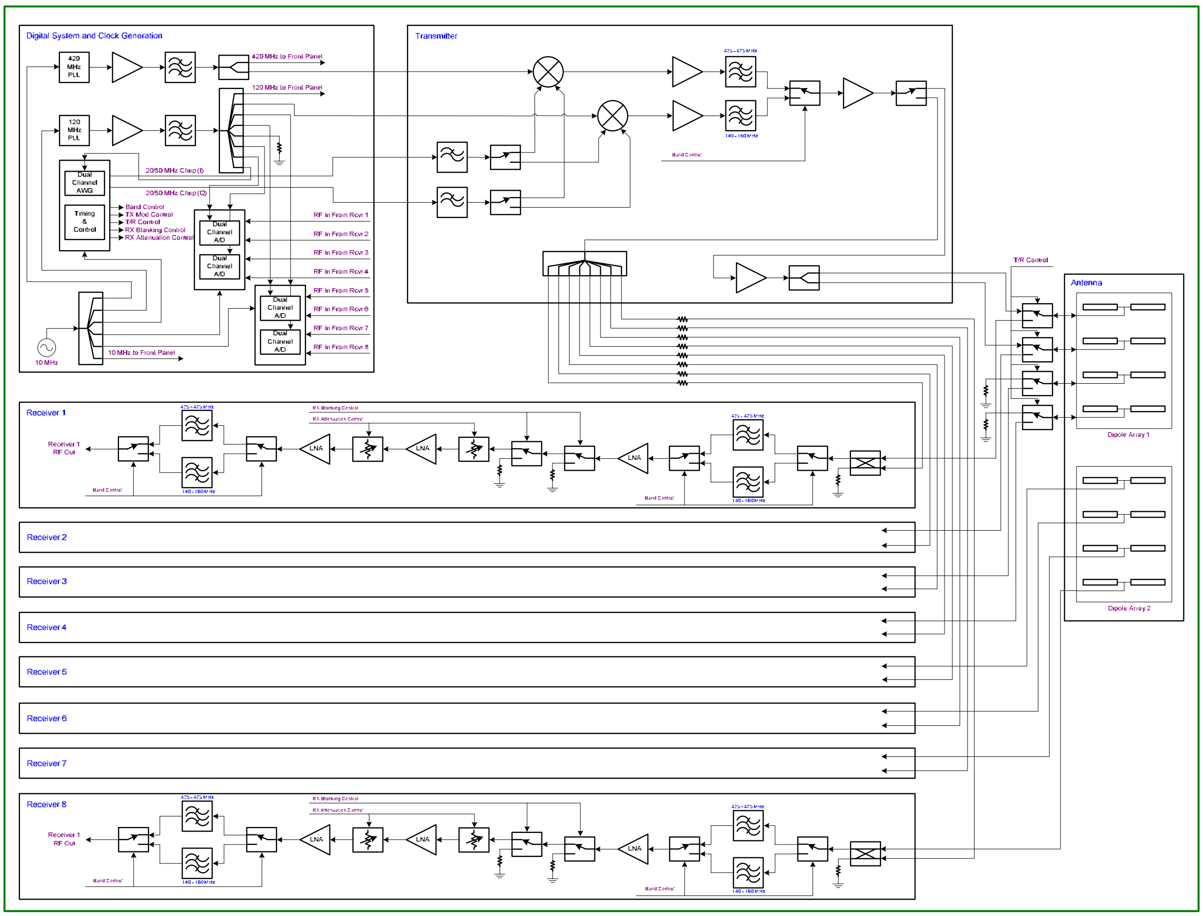

Figure 4.1.1 Block diagram of the GISMO radar

The RF sub-system is composed of a transmitter module that operates at the center frequencies of 150 MHz and at 450 MHz, and 8 receivers that operate at both frequencies.

The frequency-synthesizer sub-system generates local oscillator (LO) signals for the higher and lower bands of the radar, and it is implemented on a single printed circuit board with filters to eliminate spurious signals. This design has been used successfully in the Multi-Channel Radar Depth Sounder (MCRDS).

The digital sub-system consists of an Arbitrary Waveform Generator (AWG) for generating the baseband chirp waveforms, analog-to-digital converters (ADCs) and a timing and control module for generating the control signals needed for radar operation.

The antenna section consists of 8 dipole antennas divided into 2 dipole arrays. The flow of signals to the dipole array 1 is controlled by a duplexer (high power T/R switch), which switches to “transmit” and “receive” modes based on the T/R control signal.

4.2 RF Section

The RF section has major blocks identified as Transmitter and Receiver.

Transmitter

Figure 4.2.1 shows the elements of the transmitter sub-system. The baseband in-phase (I) and quadrature (Q) chirp signals from the AWG are low-pass filtered to reduce any out-of-band signals. These filtered signals are then sent to an image-reject mixer to up-convert them to 140-160 MHz and 425-475 MHz bands. The up-converter output is then passed through an amplifier and bandpass filtered to eliminate harmonics and intermodulation products generated by mixers in the up-converter. The bandpassed signals are further amplified with a driver amplifier. A high-power amplifier amplifies the output signal from the driver amplifier to about 300 W and the high-power amplifier output is applied to the transmit antenna. A part of the transmit signal is applied to an 8-way power divider and fed into the receiver sub-system for calibrating the system.

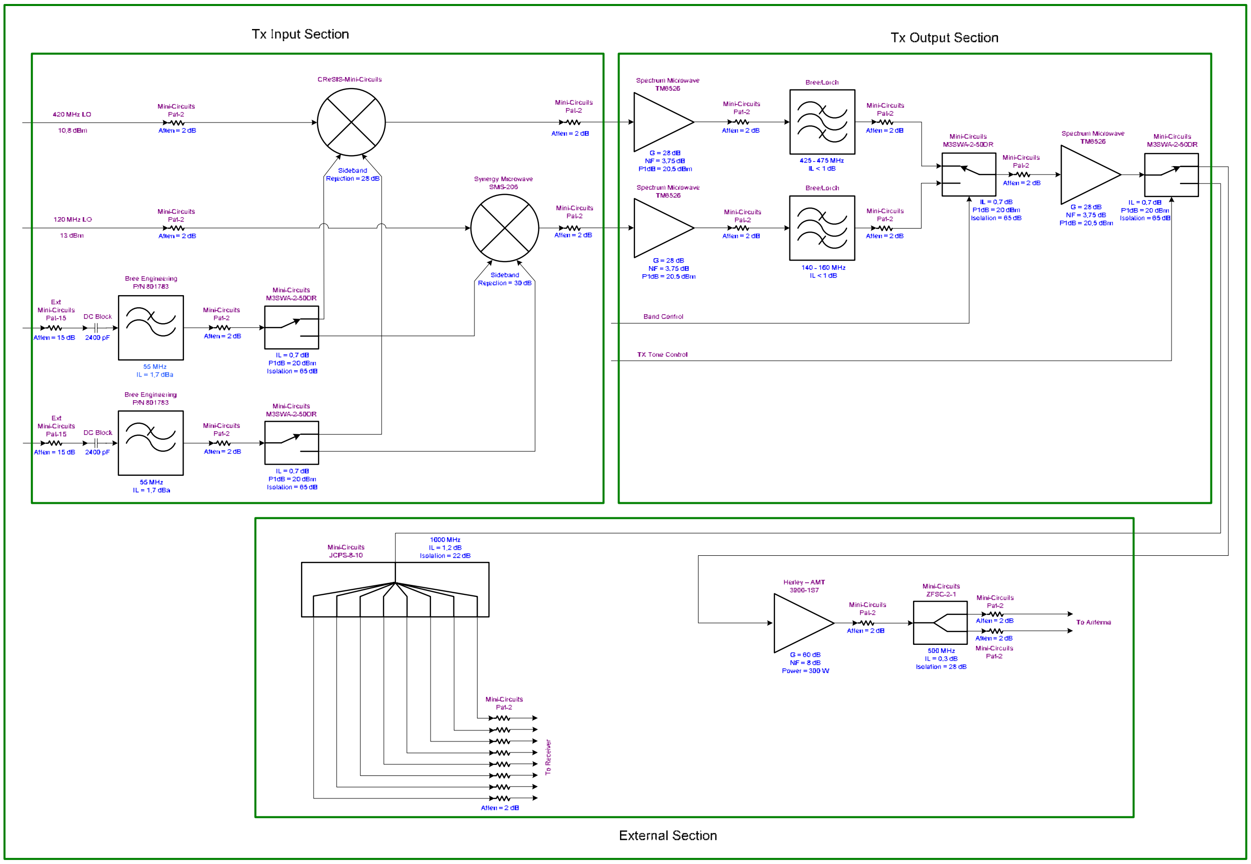

Figure 4.2.1: GISMO Transmitter

Receiver

The receiver sub-system is designed to operate both at 150 and 450 MHz. It consists of 8 identical receivers — one receiver for each element of an 8-element dipole antenna array. Figure 4.2.2 shows the receiver block diagram. Each receiver front-end consists of a directional coupler that is used to inject a sample of the high-power signal from the transmitter into the receiver for calibration. The received signal from the antenna is supplied to a low-noise amplifier through the directional coupler main port, two receiver single-pole double throw (SPDT) and a bandpass filter. The SPDT switches are used to select the frequency band of operation. The output from the low-noise amplifier is passed through a couple of SPST switches, which are used to blank the receiver during transmission. The output from the blanking switches is further amplified and filtered before digitization. Each receiver includes a digital attenuator to set the receiver gain. The blanking switches and the attenuator are programmed to prevent receiver damage and saturation.

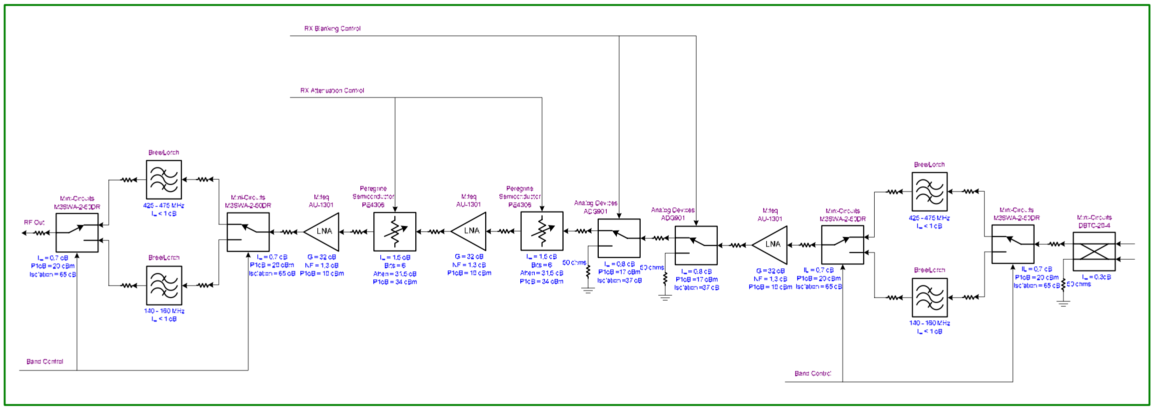

Figure 4.2.2: GISMO Receiver

4.3 Digital Section

The digital section consists of an AWG constructed with Field Programmable Gate Arrays (FPGAs) to generate a base-band chirp signal. This section also hosts a 12-bit ADC for digitizing the receiver output.

Frequency Synthesizer Section

The frequency synthesizer board generates a 120-MHz and 420-MHz LO signal at a power level suited to meet the transmitter specifications.

Figure 4.3.1 shows the block diagram of the frequency synthesizer.

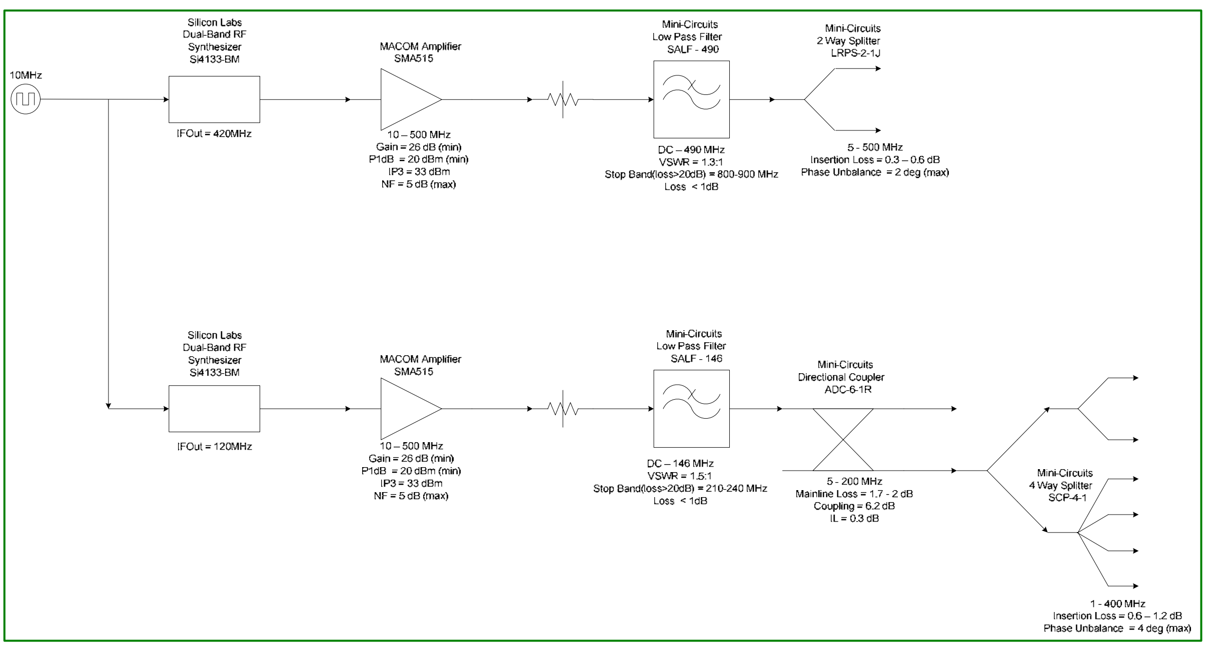

Figure 4.3.1: Frequency Synthesizer

Following are the system level specifications of the RF chain of the Phased Locked Loop (PLL) Board.

The frequency synthesizer generates a 120-MHz signal that is distributed to the following sections of the radar:

- The local oscillator used for mixing the Intermediate Frequency (IF) and the RF signals in the transmitter section;
- The Arbitrary Waveform Generator;
- The Data Acquisition System.

The receiver down-converts the signals and samples it at a rate of 120 MHz. A 64- macrocell Complex Programmable Logic Device (CPLD) is used to program both the synthesizers with their respective lock frequencies (120 MHz and 420 MHz).The CPLD has been programmed using Very High-Speed Integrated Circuit Hardware Description Language (VHDL). The power on reset chip is designed with a pulse repetition period of 2 s to allocate enough time for the CPLD to drive the frequency synthesizer chips and reach a steady state. When the two chips lock to their respective frequencies, the Light Emitting Diodes (LEDs) are turned on through the control signals from the CPLD. The clock oscillator connected to the CPLD is disabled when the lock occurs.

The output signal of both the frequency synthesizer chips then passes through the RF chain. As indicated by the link budget calculations in Section 4.5, the amplifier and the splitters are used to attain the desired power levels at each output node. The low pass filter is used to pass the desired frequency and ensure that the harmonics are suppressed sufficiently.

4.4 Antennas

The GISMO project is upgrading the existing VHF radar antenna arrays. These antennas were developed for operation at the center frequency of 150 MHz and consist of 4 dipoles, each about 1 m in length, mounted 0.5 m below each wing of an aircraft. The 1-m length and 0.5 spacing below the wing corresponds to a half-wavelength dipole mounted at a quarter-wavelength distance from a ground plane. The aircraft wings have a tilt of about 6°-above-horizontal, which points the antenna beam 6° off nadir when the array is fed in phase. We are planning to use the same antenna arrays at 450 MHz. At this frequency, the dipole will be close to 3 wavelengths along the ground plane and three quarters of a wavelength from the aircraft wing. Figures 4.4.1 and 4.4.2 show the mounting of the dipole antenna array below the aircraft wings.

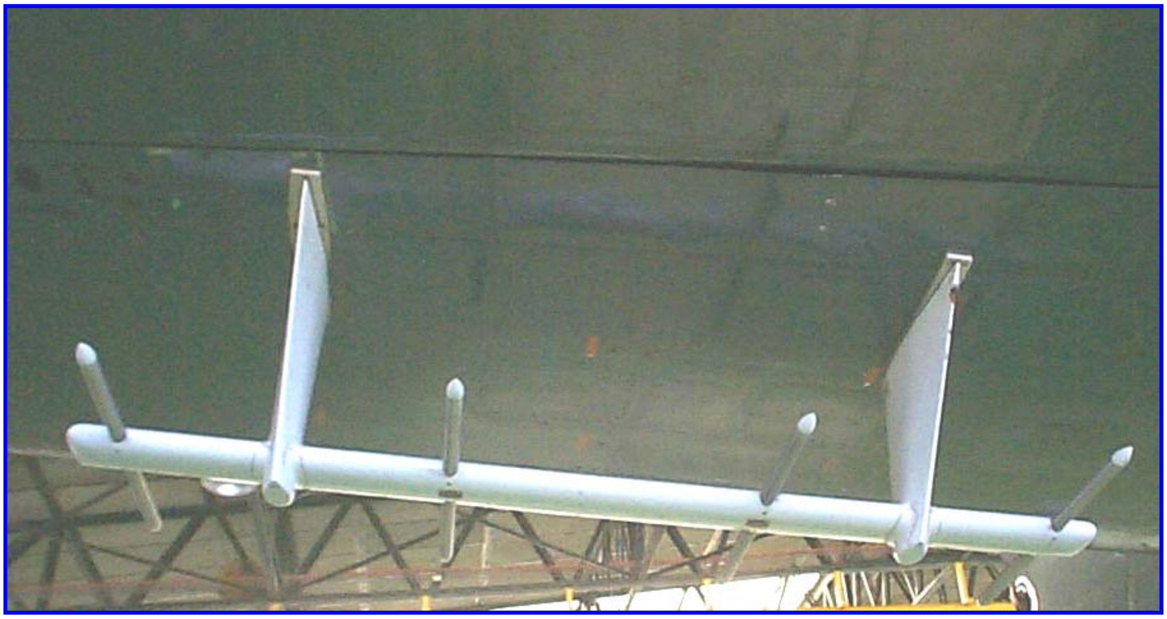

Figure 4.4.1: Dipole Antenna Array Mounting

Figure 4.4.2: Dipole Antenna Array Mounting

4.5 Project Progress

RF Sub system

We started the development of the transmitter input section first. Since suitable higher band modulator was not available in-house, we developed a single sideband (SSB) mixer. Figure 4.5.1 shows the block diagram of this mixer.

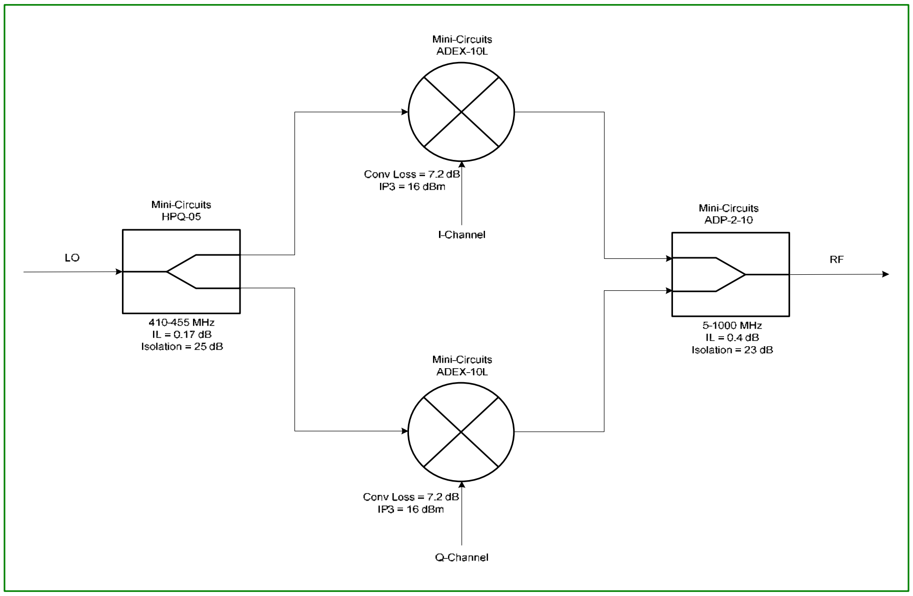

Figure 4.5.1: Single Side-Band Mixer

The upper-sideband converter was developed using an in-phase and a quadrature power divider/combiner and two mixers. Using a 3-dB quadrature power divider, the input signal at 420-MHz is split into two parts and supplied to the mixers' local oscillator port. The I and Q signals from the AWG in the frequency range 5-55 MHz are applied to the mixers' IF ports. The output signals from the mixers' RF ports are summed using an in-phase power combiner to obtain the upper-sideband signal over the frequency range from 425 to 475 MHz. The lower sideband is suppressed by 28 dB. Figure 4.5.2 shows the schematic of the single-sideband up-converter used to generate the PCB layout.

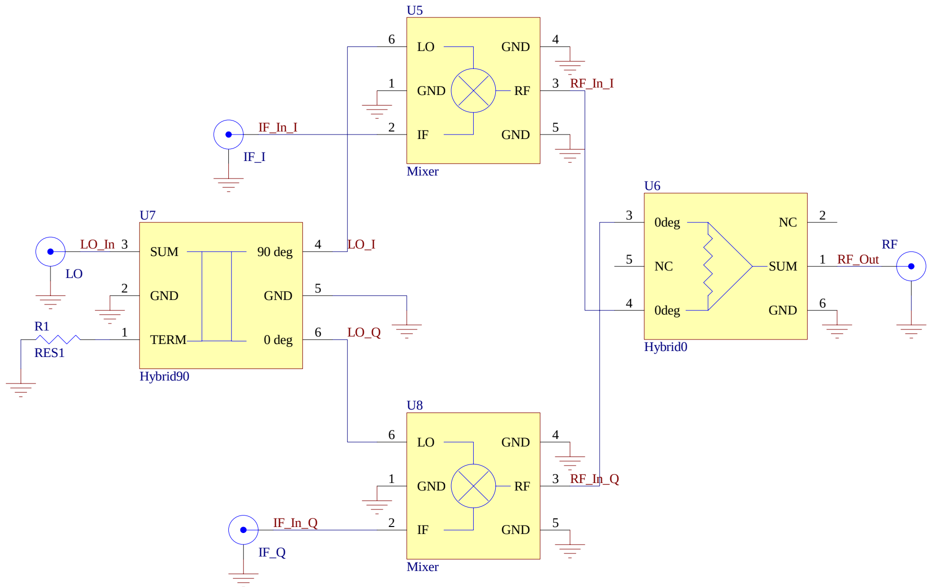

Figure 4.5.2: Schematic for Single Sideband Mixer

Next we developed the transmitter input section. Figures 4.5.3 and 4.5.4 show the schematics of input and output sections, respectively. We used these schematics to generate the PCB layout.

We are planning to characterize individual components used in the radar system and perform co-simulation on Agilent Technologies', Advanced Design System (ADS) to identify any problems and optimize the performance before fabricating PCBs of each section.

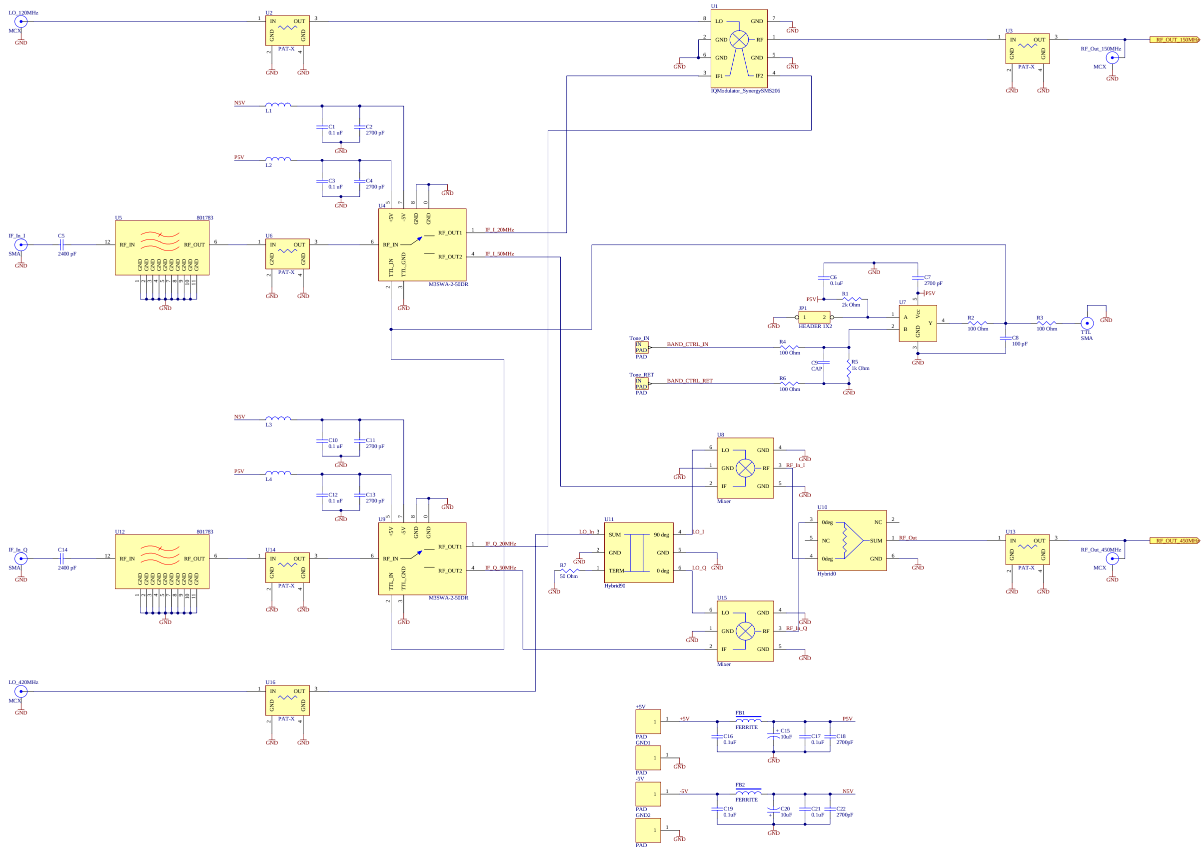

Figure 4.5.3: Transmitter Input Stage Schematic

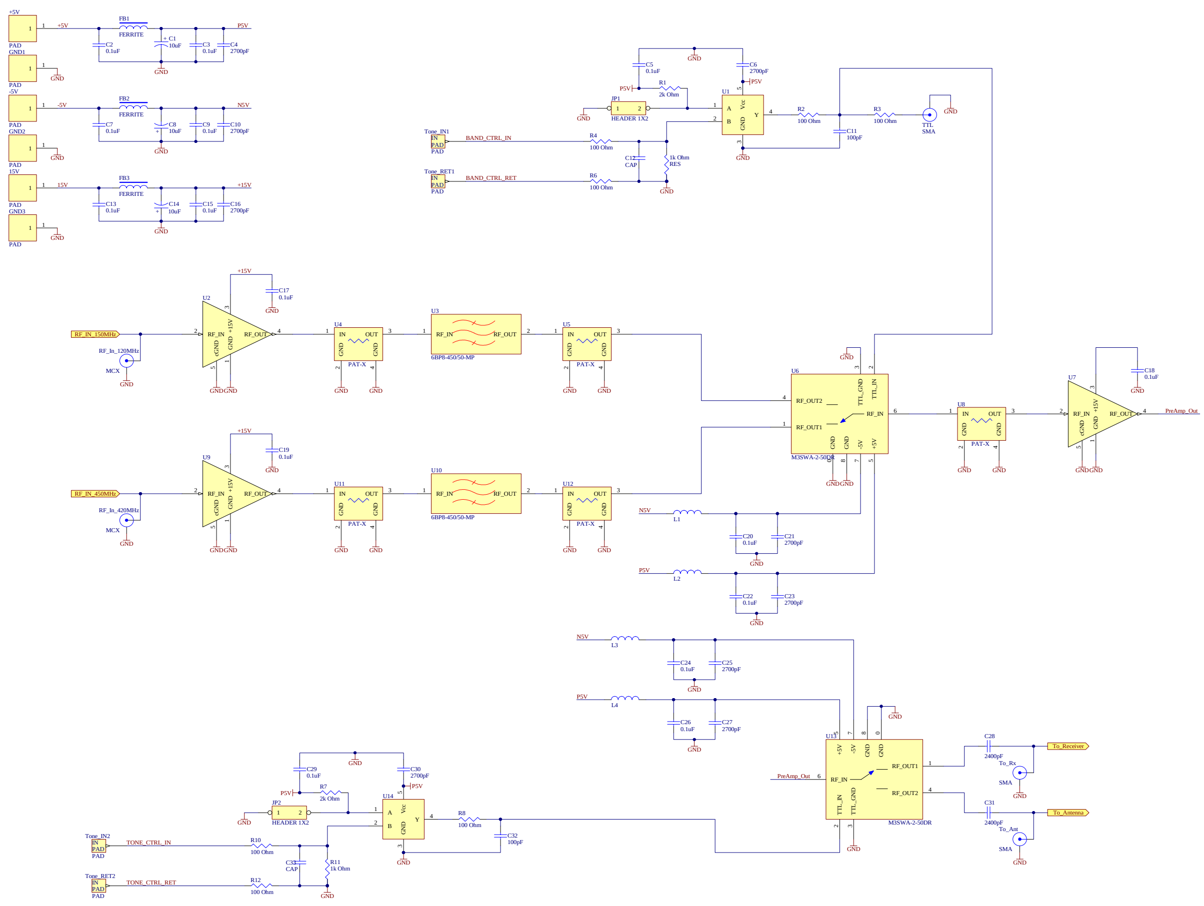

Figure 4.5..4: Transmitter Output Stage Schematic

Frequency Synthesizer Section

Figure 4.5.5 shows the schematic for the frequency synthesizer.

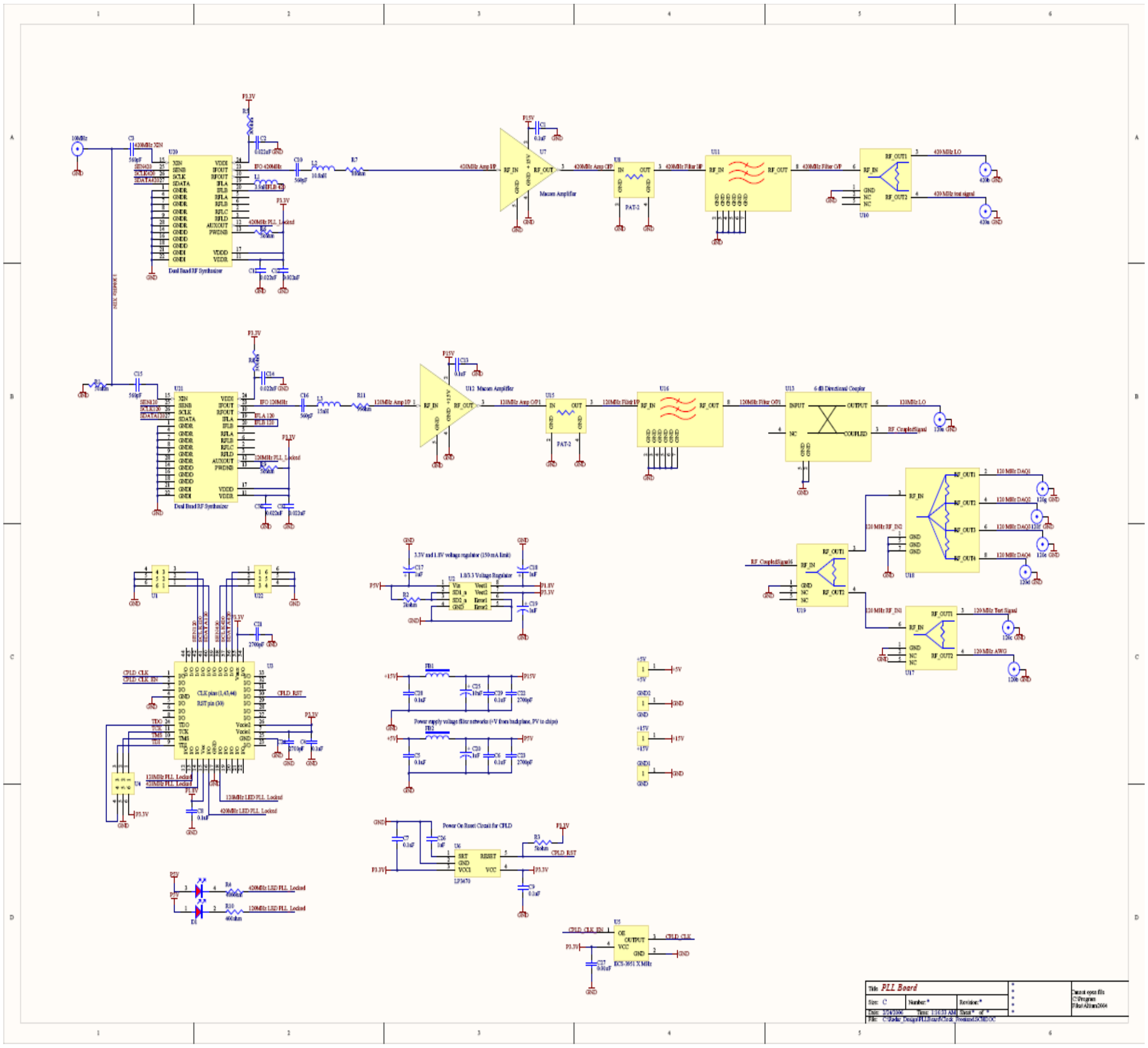

Figure 4.5.5: Frequency Synthesizer Schematic

We have done an extensive characterization of the frequency synthesizer and associated circuitry. The output power of the synthesizer is shown in the link budge table 4.5.1 and 4.5.2 at 120 and 420 MHz respectively. Test results are shown in tables 4.5.3 and 4.5.4. We also tested variation of the lock frequency with input and the test results are shown figures 4.5.6 and 4.5.7. Both the figures indicate that the respective frequencies lie in the middle of the tuning range of the PLL.

Link Budget

Si4133-BM	SMA 515	PAT-2	SALF-490	Splitter		Output
				IL	*Atten*	
-8	26	-2	-1	-1.2	-3	**10.8**

Table 4.5.1: Power levels in dBm for 420 MHz

Si4133-BM	SMA 515	PAT-2	SALF-146	Coupler		Splitter 1st level		Splitter 2nd level		Output	
				ML	*Coupling*	*IL*	*Atten*	*IL*	*Atten*		
-8	26	-2	-1	-2.1						**12.9**	*To LO*
					-6	-0.6	-3	-0.6	-3	**1.8**	*AWG,TP*
								4-Way Splitter			
								-1.2	-6	**-1.8**	*DAQ(4)*

Table 4.5.2: Power levels in dBm for 120 MHz

Testing

Point of Measurement (SMA/MCX)	**Power Output (dBm)** (experiment results)	**Power Output (dBm)** (worst case theoretical values)
To LO	16.8	12.8
DAQ1	2.4	-1.8
DAQ2	2.4	-1.8
DAQ3	2.4	-1.8
DAQ4	2.36	-1.8
AWG	5.5	1.8
Test point	5.5	1.8

Table 4.5.3: Value of the output power levels at 120MHz

Point of Measurement (SMA/MCX)	**Power Output (dBm)** (experiment results)	**Power Output (dBm)** (worst case theoretical values)
To LO	13.1	10.8
Test point	12.9	10.8

Table 4.5.4: Value of the output power levels at 420MHz

Lock Frequency

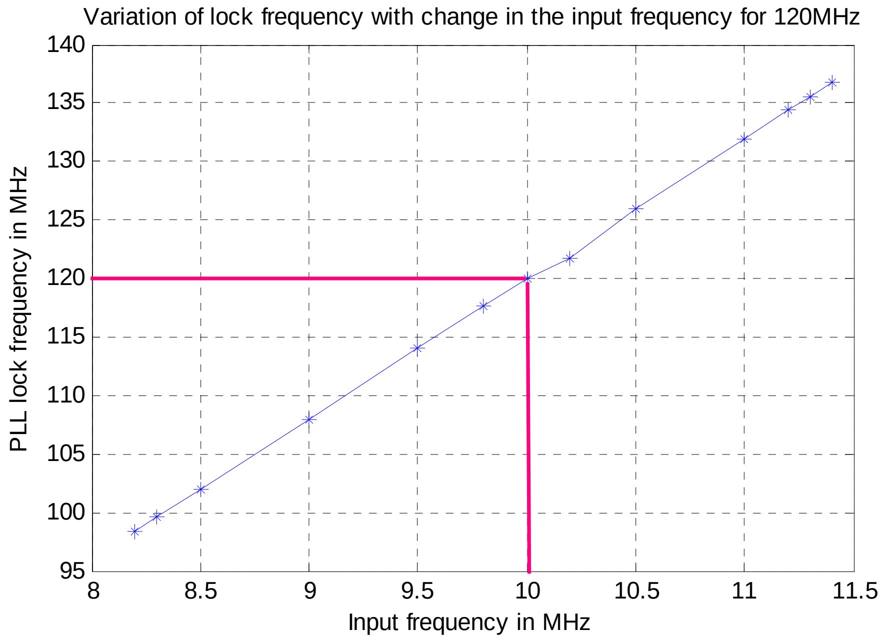

Figure 4.5.6: Variation of Lock Frequency for 120 MHz

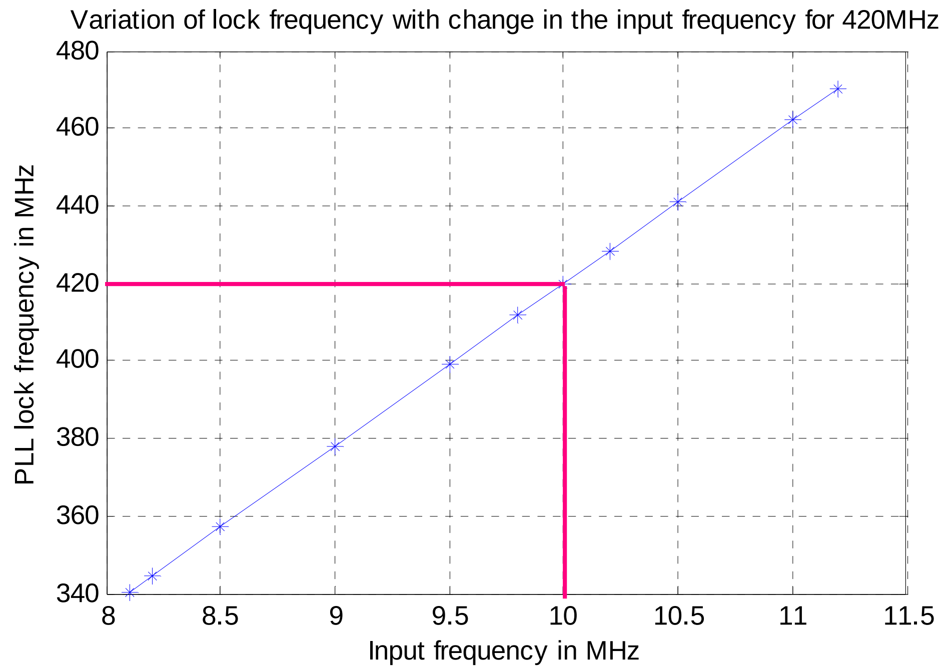

Figure 4.5.7: Variation of Lock Frequency for 420 MHz

Antenna Section

We have been conducting simulations using the software High Frequency Structure Simulator (HFSS) version 9.1, based in a computer with 1 MB-Ram at 2.4 GHz CPU, to study the 4-elment antenna array response at the 450 MHz frequency. The strategy chosen is the following:

- Generate a single dipole fixed ($\lambda c/2$= 1 m) in an infinite ground plane. (Figure 4.5.8)
- Simulate the single-dipole antenna to achieve the total radiation pattern (E plane) (Figure 4.5.9) and the total directivity radiation pattern (Figure 4.5.10).
- Build the 4-dipole array antenna fixed at $\lambda c/2$= 1 m, in an infinite ground plane, to find the return loss of each dipole (Figure 4.5.11) and the total radiation pattern of the array. (Figure 4.5.12)
- Incorporate the finite ground plane at the distance of $\lambda c/4$= 0.5 m in the XZ plane to simulate the aircraft wing to compare the results with the infinite case. At this point we can infer the accuracy of our model.
- Simulate for total radiation pattern (E plane), return loss and voltage standing wave ratio (VSWR) of each dipole (i.e. S11, S22, S33, S44) sweeping the frequency from 425 MHz to 475 MHz (BW 50 MHz) (Figures 4.5.13, 4.5.14 and 4.5.15)

The next step is to simulate the real length and width (surface) of a P-3 and Twin Otter wing as a finite ground plane over the dipole array. It is very important to note that we expect more than 48 hours of continuous simulations for each iteration in this process.

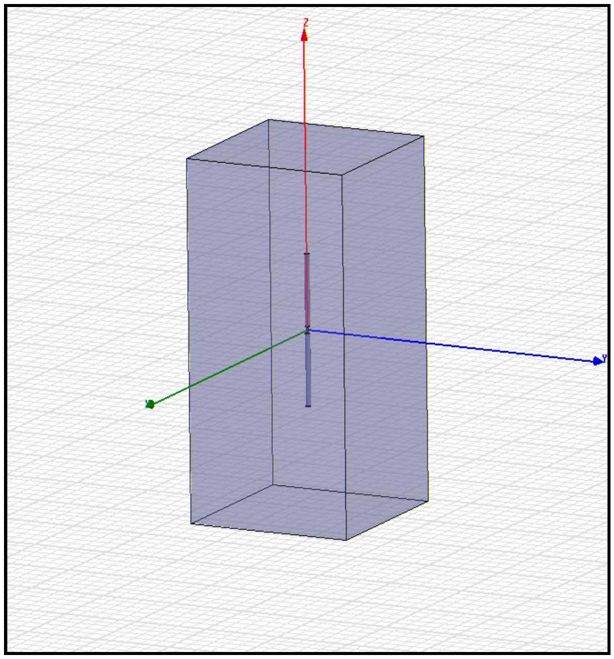

Figure 4.5.8: Single dipole fixed at λc/2= 1 m in a "near field" box

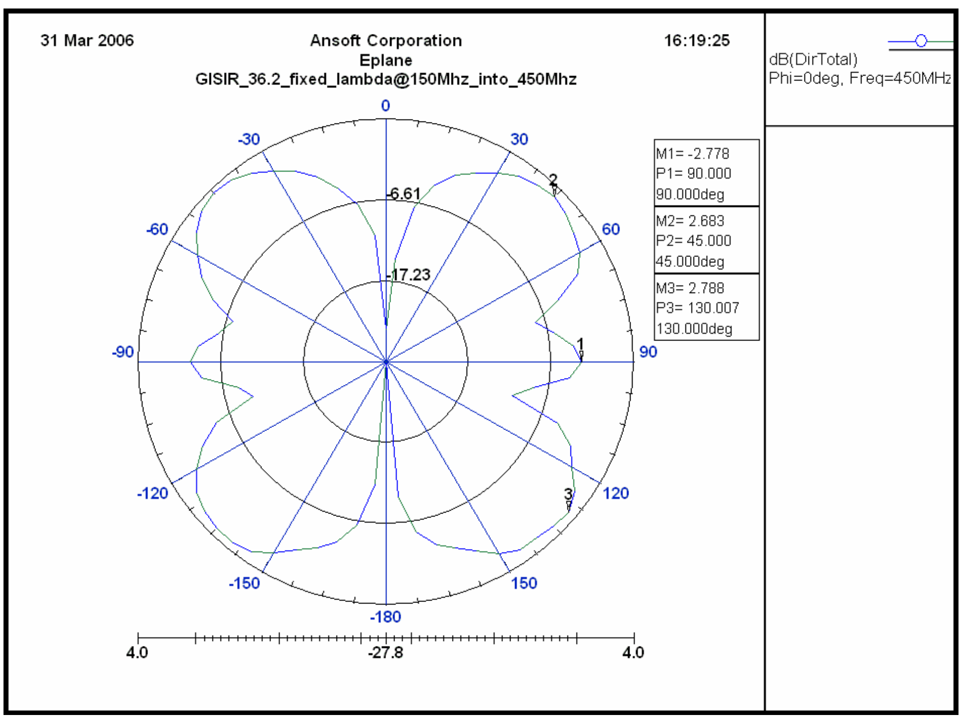

Figure 4.5.9: E plane of a Single dipole fixed at λc/2= 1 m into 450 MHz

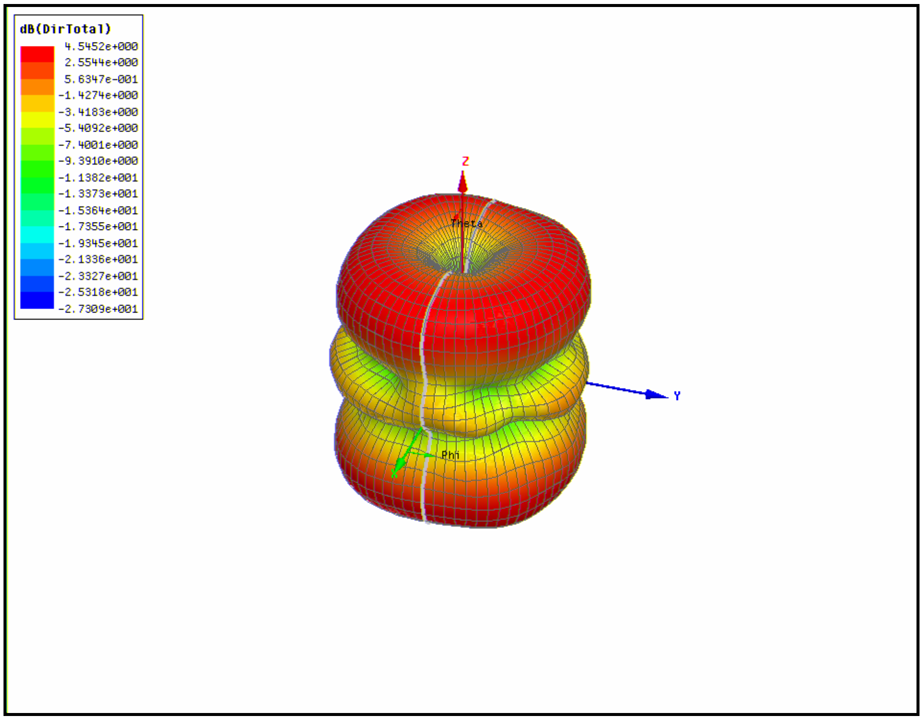

Figure 4.5.10: Directivity radiation patter of a Single dipole fixed at λc/2= 1m into 450 MHz

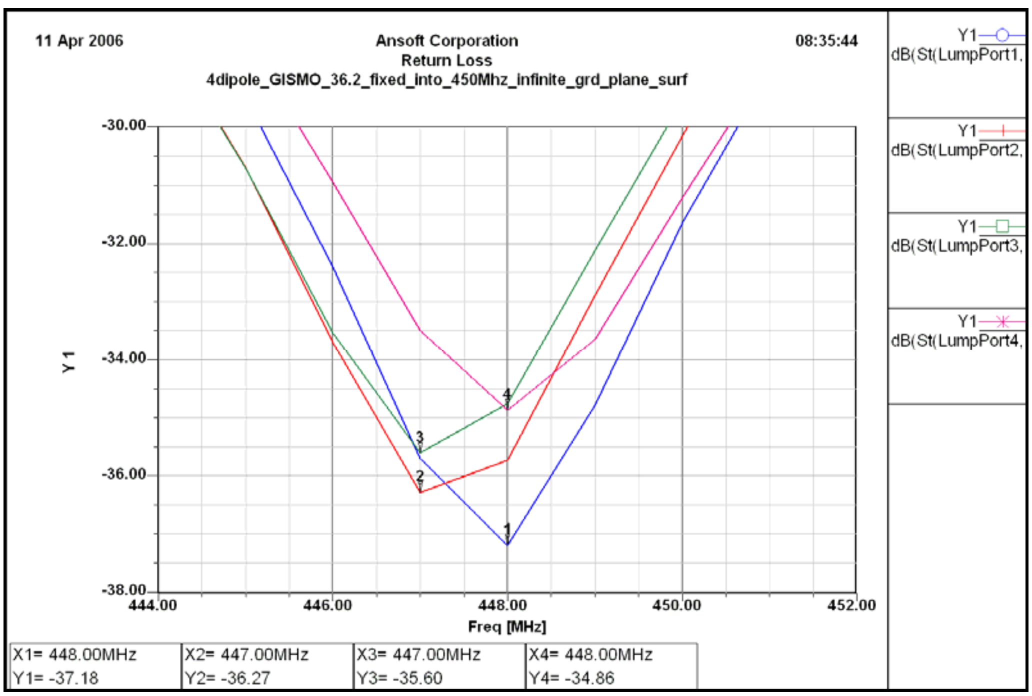

Figure 4.5.11: Infinite ground plane for return loss (S11, S22, S33, S44), fixed at λc/2= 1 m into 450 MHz

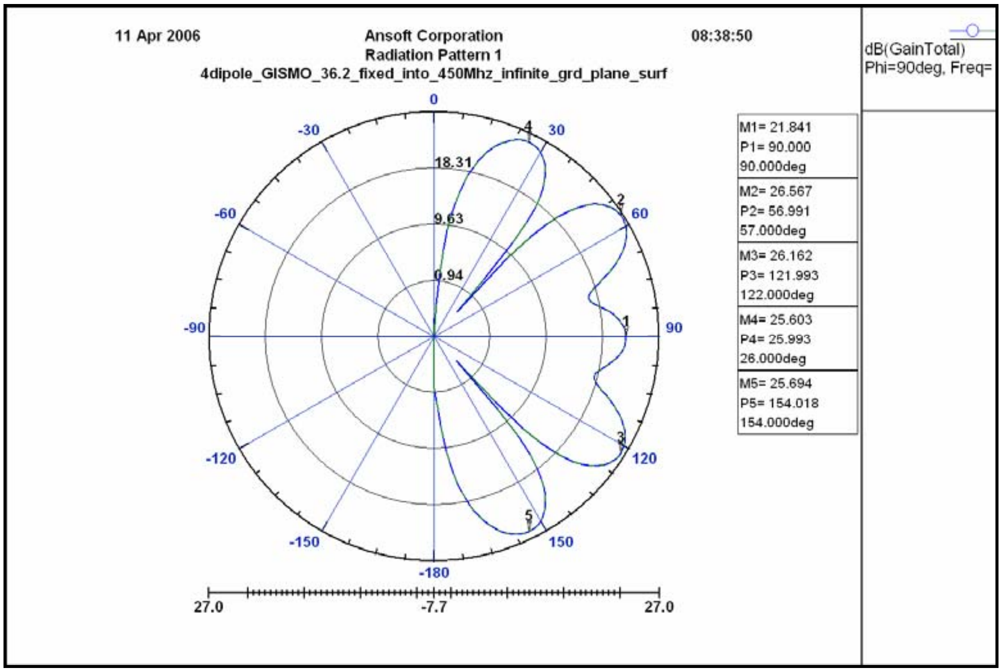

Figure 4.5.12: Infinite ground plane for total radiation pattern (E plane) fixed at $\lambda c/2 = 1$ m into 450 MHz

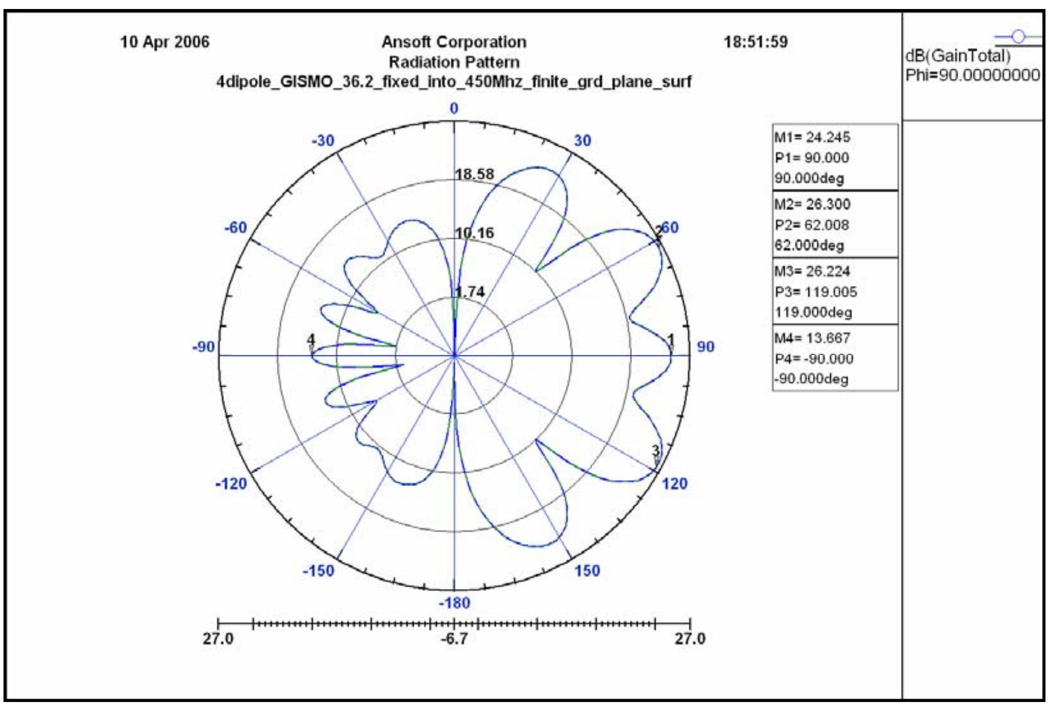

Figure 4.5.13: Finite ground plane for total radiation pattern (E plane) fixed at $\lambda c/2 = 1$ m into 450 MHz

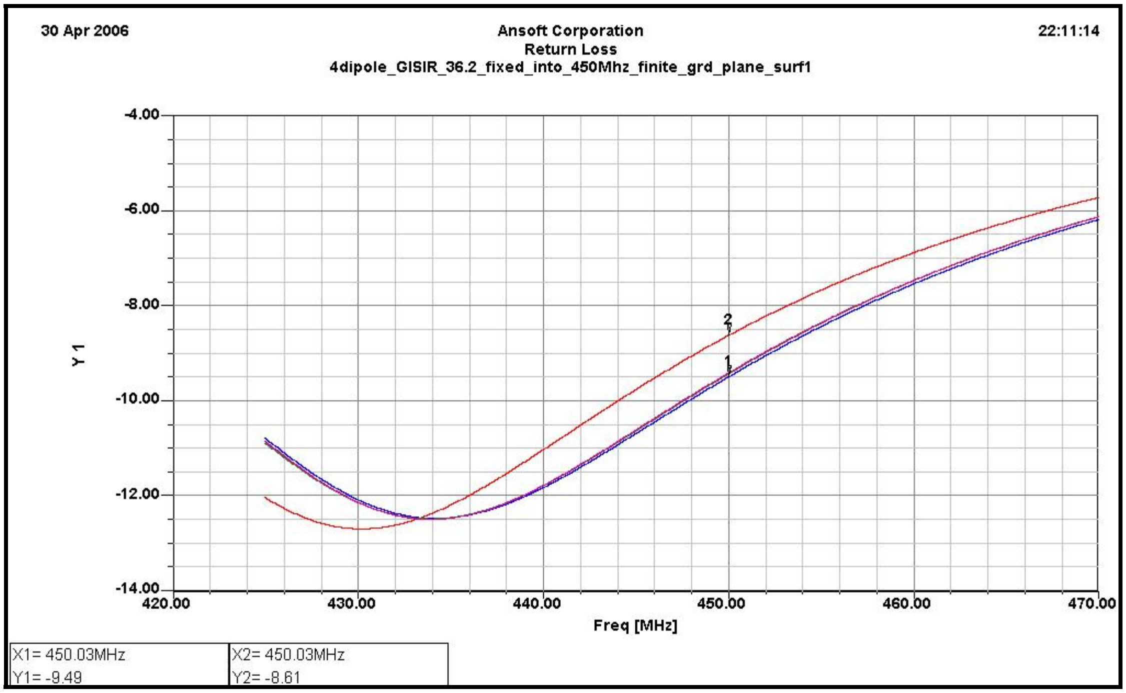

Figure 4.5.14: Finite ground plane for return loss (S11, S22, S33, S44), fixed at λc/2= 1 m into 450 MHz

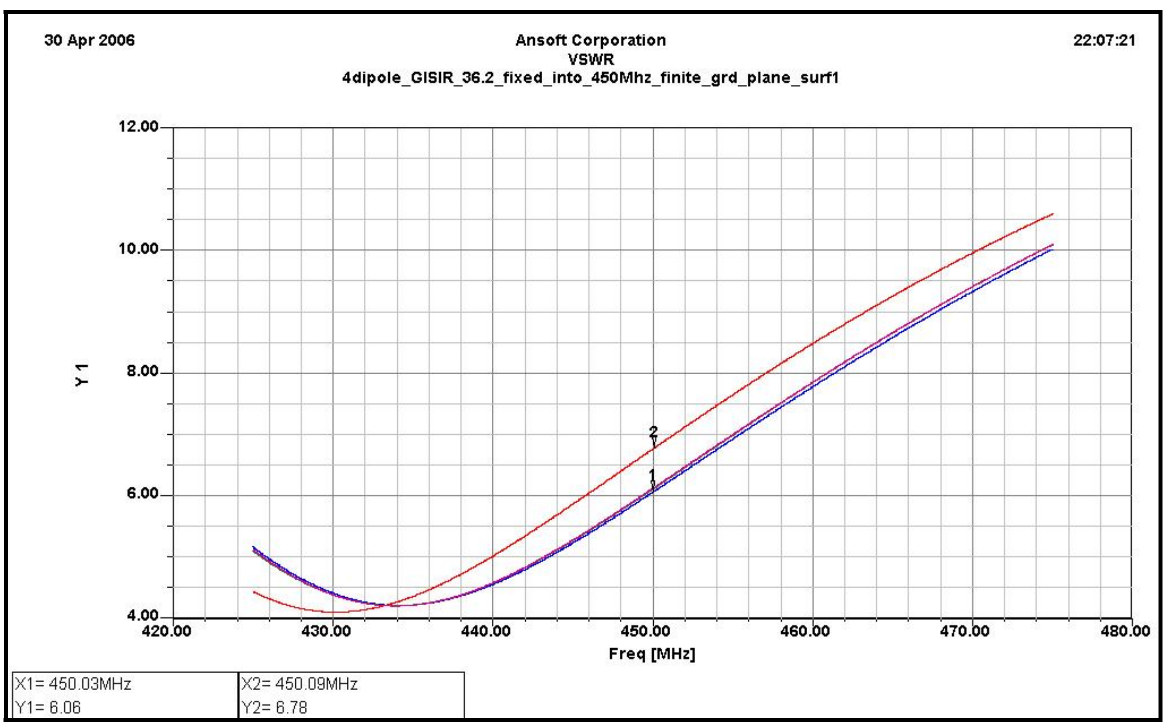

Figure 4.5.15: Finite ground plane for Voltage Standing Wave ratio (VSWR) fixed at λc/2= 1 m into 450 MHz

Discussion

The simulation results show that the VSWR of the antenna array is adequate for operating the radar at 450 MHz. However, the main lobes of a radiation pattern with a four-element array with dipoles of about 3 $\frac{\lambda}{2}$ in length are located at 60 and 120 degrees, as shown in Figure 4.5.13. The peak gain for the lobe pointed at 90 degrees is about 2 dB lower than that for the main lobes. The two-way gain loss of about 4 dB may produce minimum effect to overall radar sensitivity. We plan to conduct a more detailed study and build a scale-model to measure the gain and beamwidth.

5.0 Airborne Campaign

The primary objective of the airborne campaign is to provide experimental demonstration of the GISIR concept by collecting interferometric sounding data with a high-altitude (~10 km) airborne instrument, implementing the appropriate filtering in the processing, and comparing the results against data collected by conventional sounding at low altitude, where clutter contamination can be minimized. The secondary objectives are to examine the relative clutter rejection performance of interferometric sounders at VHF and UHF frequencies, investigate the complementary aspects of a multiphase-center tomography, and modify our spaceborne design according to our findings.

5.1 Measurement Approach

Our 150 MHz radar is ready for testing over the Greenland Ice Sheet during May 2006 The radar is mounted on a Twin Otter, which limits our maximum altitude to about 3000 m, and as of the writing of this report, one flight line has been completed. For the 2007 and 2008 flights we will implement a radar system that can operate either at 150 MHz or 430 MHz. We have proposed to use the NASA P-3 aircraft for the 2007 and 2008 experiments.

5.2 Scaling GISMO

The technique advocated for the GISIR measurement from a spaceborne platform cannot be fully scaled to an airborne demonstration. Full scaling would require scaling the ice thickness and wavelength, along with the other system parameters. However, the depth of the ice sheets cannot be controlled and scaling the wavelength cannot be accomplished without also substantially changing the penetration depth. During the past year, we calculated how the system parameters should be best scaled in an airborne experiment to demonstrate the essence of the technique, and, more importantly, acquire useful data over the ice sheets.

5.2.1 Preserving the Fringe Rate Separation

The key observation in the GISMO technique is that the interferometric fringe rate from the basal layer and the ice surface are significantly different, for a range of angles. Using the equations from Rodriguez and Wu (2006, see publication list), one finds that η, the ratio of the two fringe frequencies as a function of x_b, the cross-track distance measured at the basal layer, is given by

$$\eta = \sqrt{1 + 2\frac{H}{x_b}\frac{nD}{x_b}}$$

where H is the platform height above the ice surface, n = 1.8 is the ice index of refraction, and D is the ice sheet thickness. To demonstrate the measurement, one should preserve the same range of frequency ratios as for the spaceborne case. This implies that, given the platform height and ice thickness, the basal distance for a given frequency ratio will be given by

$$x_b = \sqrt{\frac{2HnD}{\eta^2 - 1}}$$

This implies that the cross-track distances should scales as

$$\frac{x_b}{x_b'} = \sqrt{\frac{H}{H'}}$$

Notice that this equation is independent of wavelength or interferometric baseline. If one assumes that the spaceborne GISMO measurement covered a 50 km swath from 10 km to 60 km, then by reducing the platform height from 600 km to 6 km (18,000 ft), the cross track swath should span from 1 km to 6 km in the cross track direction. Notice that the range of incidence angles at the surface will scale approximately in inverse proportion to the square root of the height

$$\frac{\tan\theta}{\tan\theta'} = \sqrt{\frac{H'}{H}}$$

In the case we considered above, the maximum incidence angle would increase from approximately from about 6 degrees to about 45 degrees. This means that in order for the full range of measurements to be possible, one must use a single dipole antenna element to transmit and receive over the entire swath. Alternately, a synthetic beam must be formed by combining the different elements and steering them electronically over the swath after individually collecting each element. This requirement translates into a requirement for separately digitizing each antenna element which is the approach we will take when operating from the Twin Otter (5-elements on each wing) and from the P-3 aircraft (4-elements on each wing).

5.2.2 Preserving the Number of Fringes

In order to mimic the ability the ability to separate the basal and ice surface fringe frequencies, one must require that the basal frequency be resolved to the same level in both measurements. This implies that the number of fringes over the swath must be preserved. The number of fringes over the swath is approximately given by

$$\Delta\Phi = kB\Delta\sin\theta \approx kB\Delta\tan\theta$$

Since we have seen that tan θ will scale as the square root of the platform height, and since we wish to preserve the wavelength, this requirement states that the baseline must scale as

$$\frac{B}{B'} = \sqrt{\frac{H}{H'}}$$

For the spaceborne GISMO design, the baseline was at least 45 m, which implies that it must be at least 4.5 m for the airborne design. Since the swath may be somewhat reduced due to the antenna illumination, and since for the airborne measurements it is desirable to demonstrate a higher accuracy, a longer baseline will chosen in practice. Note that reducing the baseline increases the elevation error implying that we can optimize our results by flying at a higher elevation. This fact along with better platform stability at higher elevations argues in favor of the P-3 aircraft.

5.2.3 Preserving the Geometric Correlation

One of the main constraints in the design of a radar interforometer is that the change of interferometric phase over a single range resolution cell must be much less than 1. The relevant ratio that determines the amount of phase wrap over a range cell, aside from constant factors, such as the wavelength, is given by

$$\frac{B}{\Delta f H \tan\theta}$$

where Δf is the system bandwidth. Given the dependence of baseline and incidence angle on height derived above, one must have that in order to retain the same level of correlation or better, the bandwidth must scale as

$$\frac{\Delta f}{\Delta f'} = \zeta \frac{H}{H'}$$

so that keeping the geometric correlation constant would require an increase of at least 100, from 6 MHz to 600 MHz, which is not feasible with the current hardware. A less stringent requirement is that the number of phase wraps over a pixel must be much less than π, without trying to preserve the same level of geometric correlation. This requirement translates to the following requirement for the bandwidth

$$\Delta f \gg f \frac{B}{x_b}$$

Assuming f = 450MHz, B < 20 m, and x_b = 1 km, then one must have that _f >> 9 MHz (~3 MHz bandwidth at 150 MHz). For the May 2006 Twin Otter flights, we will operate a 150 MHz radar with 20 MHz bandwidth. For 2007 and 2008, we will also operate a 450 MHz radar with 80 MHz bandwidth.

5.2.4 Preserving the Number of Samples per Swath

An alternate requirement on the system bandwidth is given by the desire to preserve the number of samples per swath. The number of range samples is linearly proportional to the bandwidth. The swath, on the other had goes down as the square root of the height ratios. Therefore, the number of samples per swath will be preserved if the bandwidth also scales as the square root of the height ratio. For the scaling we have been considering, this implies that the bandwidth should be on the order of 60 MHz at 450 MHz.

5.3 Navigation and Attitude Control

Navigation and attitude control information will be obtained from GPS and INS units installed on the aircraft and at fiducial points on the ground. GPS data acquisition and analysis will be carried out by EG&G and the Wallops Flight Facility. WFF has almost 20 years of experience in precision determination of aircraft position and attitude.

5.4 Airborne Experiment Definition

Our primary objectives for field tests are: verify that we can detect fringe rate separation between the surface and basal signal; verify that we can use fringe rate separation to perform clutter rejection; measure basal topography; investigate how we can use differences in basal reflectivity to characterize the properties of the bed; compare interferometric and tomographic imaging approaches; evaluate UHF and VHF performance.

We can only transmit on at one frequency at a time. Therefore we generally plan to operate at one frequency on the outbound leg of a flight line. Inbound, we will retrace the flight line and operate at our second frequency. We plan two modifications to that plan. First, we plan to fly several closely spaced (20 m) segments for use in evaluating tomographic concepts. As of the time of writing of this report, we have tested repeat pass flights with the Twin Otter. Second, we will re-fly at least one segment at the beginning and end of the experiment period (about 1 week) to determine whether there is sufficient coherence over that time period to allow for repeat pass interferometry. We will also plan to re-fly at least one flight line in 2007 and 2008 to verify any expected improvements in system performance and to evaluate whether or not repeat pass inteferometry is possible over a longer time interval

5.4.1 May 2006 IIP Experiment

As of the writing of this report, we are performing experiments over Northwest Greenland in collaboration with ongoing Wallops Flight Facility. The flight path for our test, shown in figure 5.4.1 , begins at the margin and passes over Camp Century, which is the site of numerous past radar experiments. The flight continues into the ice sheet interior. The primary objective of the May 2006 flights is to verify that fringe rate separation is detectable. We are deploying a 150 MHz radar operated from a Twin Otter aircraft. Maximum aircraft elevation will be about 10,000 ft. The flight line will extend from Thule to the interior of Greenland where, from past observations, we know the signal strength will be high. We will offset the flight track on the return flight by 20-30 m to provide additional data with a larger baseline.

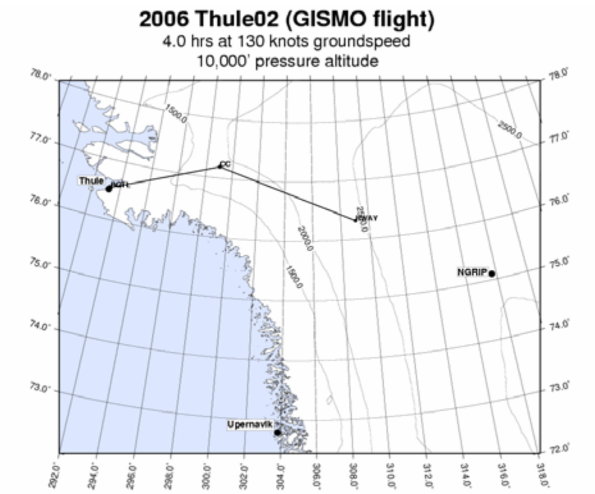

Figure 5.4.1. May 2006 GISMO Twin Otter flight over Northwest Greenland. Flight path goes from Thule Airbase, across the ice margin to Camp Century (CC) and along a line towards North GRIP. Extent is limited by the range of the Otter.

6.0 Plans for the second year

6.1 Radar Hardware and Field Operation

1) Radar Development:

a) Build sub-systems and assemble the complete system such that it can be operated at 150 and 450 MHz;

b) Perform laboratory tests using delay lines to document loop sensitivity, radar waveforms and impulse response;

c) Design antennas such that they can be operated both at 150 MHz and 450 MHz by modifying the antenna length (reducing or extending as suitable);

d) Simulate an actual and a scale-model array performance; and

e) Work with the OSU group to test the scale-model to verify simulations;

2) System Integration (KU, Wallops Flight Facility, Aircraft Operator)

a) Work with WFF aircraft group to develop antennas; and

b) Install the radar and navigational equipment on a P-3 or similar aircraft and conduct flight tests over the ocean.

3) Data Collection and processing in 2006

a) Process and analyze data to be collected during the 2006 field campaign over the Greenland ice sheet.

4) Data Collection and Processing in 2007

a) Collect data over a few areas selected as a part of May 2007 field campaign over the Greenland ice sheet;

b) Process and distribute these data to other team members; and

c) Synthesize results for publication.

6.2 Simulations and Data Processing

Second year simulation and processing tasks are as follows.

(1) **Data Simulation**

- Continue to provide data simulation support for planned data acquisitions in May 2007.
- Provide simulated data for tomography analysis.

(2) **Data Processing**

- Process some of the SAR raw data acquired in May 2006 to try to confirm the interferometric clutter canceling concept and the tomography technique.
- Process some of the SAR raw data acquired in May 2007 and to do tomography application analysis.

(3) **Tomography Processing**

- The data acquired in May 2006 will be used to verify tomography technique for generating 3D volumetric images of the regions of interest in Greenland and/or in Antarctica. The methods to be tested include direct convolution back-projection from the phase history data and the method of creating 3D images from already-formed 2D complex images.

6.3 Field deployment

We plan two P-3 deployments in 2007 and 2008. The flights are designed to validate technical concepts and to conduct glaciological experiments. These flights will be carried out in coordination with other planned research flights led by Dr. William Krabill. Coordination will increase the overall science pay-off and reduce some of the burden on shared personnel.

The NASA P-3 has capabilities that are well suited to our requirements. The P-3 aircraft can operate at higher elevations than the Twin Otter which relaxes some of the requirements on antenna beamwidth. The P-3 has a larger wing span for deploying antennas and increasing the baseline. It also has demonstrated capability to include a third antenna in the tail. Most important is the P-3 ability to conduct extended missions covering many glaciological regimes. Flight duration is the most critical attribute for attaining our science objectives.

We plan technical validation and science experiments. The May 2007 will concentrate on northern Greenland. We will test the concept at both 450 and 150 MHz. We will perform several closely spaced (20 m) repeat segments for acquiring tomographic data and to test the behavior of the interferometric system at various baselines. At the end of the experiment we will repeat the first flight segment to test for coherence over a several day period. We plan science observations along flight lines connecting the Greenland deep-borehole sites (Camp Century, GISP/GRIP, NGRIP, and the proposed NEME site). We will acquire data on basal topography, reflectivity, and using the nadir capability of the radar, internal layers. Connecting the deep borehole sites is important for better interpreting the climate signature preserved within the ice cores. We will overfly the proposed European NEME drilling site to assist in borehole site selection. We will make extensive observations along and across the NE Ice Stream. There is substantial evidence to suggest that there are transitions from wet to frozen based ice in this area. Mapping these transitions is important for understanding ice stream dynamics.

Year	**Validation Objective**	**IPY Science Objectives**
2007	Verify fringe rate separation concept at 150/450 MHz	Acquire bed topography and reflectivity data along line connecting Camp Century GISP/GRIP, NGRIP and proposed NEME deep borehole sites
2007	Compare signal strength at 150/450 MHz	Investigate distribution of subglacial water across and along North East Ice Stream
2007	Verify clutter rejection concept over smooth and rough target areas	
2007	Investigate tomography with close repeat tracks	
2007	Investigate repeat pass (several day) InSAR	
2008	Verify modifications from 2007 'lessons learned'	Bed topography and reflectivity along and across Jacobshavn Glacier to investigate controls on fast glacier flow
2008	Investigate one-year repeat pass interferometry by reflying a 2007 flight line	Bed topography and reflectivity along a line from DYE-3 to GRIP/GISP deep borehole sites
2008		OSU cluster sites overflight

6.4 Scattering Models

A key science objective is to use basal reflectivity maps to identify liquid water at the glacier bed. We plan to investigate the sensitivity of GISIR for detecting water layers by constructing 3 layer scattering models (ice, water, rock). We will use the Kirchoff model for the calculations. We plan to modify physical parameters such as rms roughness, correlation length, water layer thickness and rock permittivity as part of the sensitivity analysis.

7.0 Publications and Presentations

Rodriguez, E., A. Freeman, K. Jezek, and X. Wu (2006). A New Technique for Interferometric Sounding of Ice Sheets. EUSAR 2006, Electronic Proceedings, 6th Annual European Conference on Synthetic Aperture Radar, May, 2006, Dresden Germany, ISBN 978-3-8007-2960-9

Jezek, K., E. Rodriguez, P. Gogineni, A. Freeman, J. Curlander, X. Wu, C. Allen, W. Krabill, J. Sonntag (2006). Glaciers and Ice Sheets Mapping Orbiter Concept. EUSAR 2006, Electronic Proceedings, 6th Annual European Conference on Synthetic Aperture Radar, May, 2006, Dresden Germany, ISBN 978-3-8007-2960-9

Gogineni, S., J. Paden, T. Akins, C. Allen, D. Braaten, and K. Jezek (2006). Wideband synthetic aperture radar imaging of sub-surface interfaces in glacial ice. EUSAR 2006, Electronic Proceedings, 6th Annual European Conference on Synthetic Aperture Radar, May, 2006, Dresden Germany, ISBN 978-3-8007-2960-9

Jezek, K., E. Rodríguez, P. Gogineni, A. Freeman, J. Curlander, X. Wu, J. Paden, and C. Allen (2006), Glaciers and Ice Sheets Mapping Orbiter concept, J. Geophys. Res., 111, E06S20, doi:10.1029/2005JE002572.

Rodriguez, E., and Wu, X. Interferometric ice sounding: a novel method for clutter rejection, submitted to IEEE Trans. Geoscience and Remote Sensing, 2006.

Jezek, K.C. , The Future of Cryospheric Research. Byrd Polar Research Center Colloquy, The Ohio State University, Columbus, Ohio, October, 2005.

Jezek, K.C., Spaceborne Observations of Antartica: The RAMP and GISMO Project. USRA Lecture Series, University of Alaska, Fairbanks, October 2005.

Curlander, J., K. Jezek, E. Rodriguez, A. Freeman, P. Gogineni, J. Paden, C. Allen, X.Wu. Glaciers and Ice Sheets Mapping Orbiter. Advanced SAR Workshop, Montreal, Quebec, 2005.

Forster, R., Jezek, K., E. Rodriguez, S. Gogineni, A. Freeman, J. Curlander, X. Wu, C. Allen, P. Kanagaratnam, J. Sonntag, W. Krabill, "Global Ice Sheet Mapping Orbiter" , FRINGE 2005 Workshop, Advances in SAR Interferometry from ENVISAT and ERS missions", European Space Agency, ESRIN Frascati, Italy 28 November - 2 December 2005

Jezek, K., E Rodriguez, P. Gogineni, A. Freeman, J. Curlander, X. Wu, C. Allen, P. Kaagaratnam, J. Sonntag, and W. Krabill. Glaciers and Ice Sheet Maping Orbieter, EOS Trans., AGU, 86(52, Fall Meet. Suppl., Abstract IN13B-1092.

Jezek, K., The Global Ice Sheet Interferometric Radar. CReSIS Research Seminar, University of Kansas videoconference, April, 2006.

8.0 Year 2 Budget

Sarlaries and Wages			
Senior Personnel			
K. Jezek (3 mo/yr)		$33,761	
Other Personnel			
Grad Student (12 m)		$17,304	
Clerical Support(1 m)		$3,914	
Fringe Benefits			
Regular Appt. 26.80%	$9,048		
Student Appt. 10.9%		$1,886	
Other Appt. 34.40%	$1,346		
Salaries Wages and Fringe Benefits			**$67,260**
Travel			
Domestic (PI for collaboration)			**$5,000**
Participant Stipends			
Stipends ($4000)	$16,000		
Travel and Subsistence ($4000)	$16,000		
Total Stipends			**$32,000**
Other Direct Costs			
Materials and Supplies			
Total Miscellaneous Supplies			**$2,000**
Subawards			
University of Kansas		$334,923	
E.G.&G.**		$33,000	
Vexcel		$85,000	
Total Subawards			**$452,923**
Other			
Tuition			**$13,800**
Total Direct Costs			**$572,983**
Total Indirect Costs			**$49,134**
49.5% (99,260)			
No indirect on participant stipends or tuition			
**Indirect on first $25,000 of each subaward only			
Total Direct and Indirect Costs			**$622,117**
Direct NASA Funding			
JPL			**$295,100**
Aircraft Costs to Wallops Flight Facility			**$150,000**
Total NASA Cost			**$1,067,217**